Geophys. J. R. astr. Soc. (1977) **51**, 275–312

Theoretical seismograms of core phases calculated by frequency-dependent full wave theory, and their interpretation

George L. Choy* *Lamont-Doherty Geological Observatory and Department of Geological Sciences, Columbia University, Palisades, New York 10964, USA*

Received 1977 March 26; in original form 1976 December 3

Summary. A frequency-dependent full wave theory is successfully employed to synthesize long-period seismograms of the core phases *SmKS* ($m = 1, 2, \ldots$) in the distance range 100°–125°. Body-wave displacements are calculated by numerically integrating in the complex ray parameter plane. Langer's method is employed to obtain a uniformly asymptotic approximation to the vertical wave functions. Plane-wave reflection and transmission coefficients are adequately corrected for the effect of the curvature at the core–mantle discontinuity by the use of generalized cosines. Results are presented in the time domain, after a numerical Fourier (inverse) transform.

The computed seismograms exhibit many non-ray effects that the *SmKS* incur upon interacting with the core–mantle boundary. For *SKS*, the amplitude, group delay and phase delay are very strong functions of frequency at less than 0.5 Hz, both because of the frequency dependence of the reflection/transmission coefficients at the core–mantle boundary, and because of the presence of diffracted energy, called *SP*(diff)*KS*, perturbing the waveform. The diffracted energy of the type that perturbs *SKS* may also interact with shear waves to give rise to a precursor to the body-wave *ScS*, called *SP*(diff)*S*. The major complication in synthesizing the portion of the seismogram containing *SmKS* for $m \geq 2$ is that the arrival time of each successively higher order reflection is within the waveform of previous lower order reflections. It is found that a summation of body-wave displacements from *S2KS* to *S15KS* gives an adequate seismogram in the distance range 100° - 125°. Each individual reflection has an amplitude spectrum, group delay and phase delay which are strongly frequency-dependent at less than 0.2 Hz. It is shown that arrival times for *SmKS*, $m \geq 2$, cannot be picked accurately by conventional methods. Furthermore, neglecting the frequency-dependence of reflection/transmission coefficients can significantly distort the interpretation of amplitude and phase data.

The seismograms generated by this method agree so remarkably well with observed records that the synthetic waveforms provide a powerful test of the validity of particular earth models. In particular, we find that the waveforms

* Present address: Office of Earthquake Studies, US Geological Survey, Denver, Colorado 80225, USA.

of *SmKS* are exceedingly sensitive to velocity gradients of the upper 200-km of the outer core, and indications are that the velocities in the outer 200-km of the core are higher, but the velocity gradient is lower, than that predicted by Hales & Roberts or earth model 1066B. The pulse widths of *SmKS* are also used to determine some fault parameters.

1 Introduction

Though the general features of currently accepted earth models are in agreement (Dziewonski 1976), there is much less agreement among models in detailing the fine structure of the Earth. Normal mode data cannot yet be used to resolve features on the order of 100 km or less (Anderson & Hart 1976). The needed resolution can be provided by the inversion of body-wave data. Body-wave techniques commonly consist of inverting travel-time data or apparent velocities. However, it is often difficult if not impossible to apply these techniques to arrivals other than the first direct body wave. Later arrivals travel non-minimum travel-time paths which may result in severely distorted waveforms (Jeffreys & Lapwood 1957; Hill 1974; Choy & Richards 1975), and their signal-to-noise ratio is reduced by the presence of body-wave codas. A relatively recent approach to body-wave data has been to construct earth models by generating waveforms which correlate favourably with actual seismograms. Two frequently used techniques of synthesizing seismograms are the Cagniard method adapted to spherical geometry (Gilbert & Helmberger 1972) and the reflectivity method (Fuchs 1968). One feature of both these methods is the assumption of an earth-flattening transformation, although the transformation law for density is not exact (Chapman 1973). Since both techniques approximate a radially inhomogeneous earth by many flat homogeneous layers, a ray with a turning point can be completely described only if all possible multiple reflections and refractions are summed. The reflectivity method accounts for the whole sum, but the Cagniard method requires, in practice, a truncation, in which case the limits of applicability (i.e. accuracy) of the truncated sum are not well understood.

An alternative technique is to perform a numerical inversion to the time domain from frequency components obtained from a frequency-dependent full wave theory. The full wave theory avoids the earth-flattening approximation and preserves the spherical geometry of the earth in describing propagating waves. A ray with a turning point need not be unnaturally decomposed into an infinite system of internal reflections and refractions within fine layering. Till recently, practical difficulties, both theoretical and economical, prevented its widespread use. The primary obstacle has been that the WKBJ approximation to the radial wave function fails, particularly at low frequencies, when the turning point of a ray is near a discontinuity. Circumventing the problem by an explicit numerical solution of the radial wave equation is possible (Chapman & Phinney 1972), but matching to the WKBJ approximation is awkward and the overall method is computationally time-consuming. Non-uniform Airy approximations may be employed to compute radial wave functions near the turning point itself, and the WKBJ approximation may be employed in regions far from the turning point, but the connection between the approximations is not well established. Neither of these approximations is uniformly asymptotic and it is not clear how to obtain a wave function employing these approximations which is accurate over all the ray parameters required (Richards 1973). Fortunately, Richards (1976) describes a formulation, the Langer method, which is uniformly asymptotic in approximating radial wave functions whether in the region of a turning point or not.

The purpose of this paper is to demonstrate that, once the Langer method is incorporated, it is not only practical, but advantageous to employ a frequency-dependent full wave theory to generate theoretical seismograms. A description of the technique in the

frequency domain and its numerical inversion to the time domain is described in the next two sections of this paper, using the body waves *SmKS* ($m = 1, 2, \ldots$) and *ScS* to illustrate the application of the full wave theory. The third section of this paper describes some salient characteristics of the *SmKS* body waves. For instance, they play a crucial role in constraining models of the outer core, yet it is nearly impossible to obtain correct arrival or differential times for higher order *SmKS* body waves. In the fourth section, the theoretical seismograms, amplitude spectra and phase spectra of these body waves are shown. The proximity of the turning points of these body waves to the core–mantle boundary give rise to effects not predicted by classical ray theory, including diffraction and frequency in reflection and transmission coefficients. It is shown that the neglect of frequency dependence can result in gross misinterpretation of the physical properties of the Earth. In the fifth section of this paper, it is shown that the correlation of synthetic and actual seismograms of deep earthquakes is so remarkable that the interpretation of the theoretical waveforms provides a powerful means of testing the validity of particular earth models. The implications for Earth structure at the core mantle boundary and the fault parameters inferred from the waveforms of *SmKS* are described.

2 Calculation of body wave amplitude and phase

The theory of rays propagating in an earth with spherical discontinuities developed initially with elementary models (e.g. Scholte (1965) who studied a fluid core embedded in a homogeneous elastic mantle). The sophisticiation of the full wave theory has since been extended to describe the fields that exist in a radially inhomogeneous but spherically symmetric earth. Chapman & Phinney (1972) computed the body-wave displacement in the frequency domain by an integral over horizontal wavenumber. Richards (1973) realized an improvement by factorizing frequency out of this wavenumber and developing a displacement integral over a line in the complex ray parameter plane. This latter form of the integral has the advantage that the saddle point is independent of frequency. Thus, any frequency component may be computed using the same path of integration. In contrast, an integral over wavenumber has a different saddle point for each frequency, and so the path of integration is not as flexible as in the ray parameter plane. The flexibility of the full wave theory used by Richards (1973) to calculate the frequency-dependent displacement due to a point source for body waves of the type *PmKP* is augmented in this paper by introducing the Langer approximation (Langer 1949, 1951) at a stage where normally the WKBJ or non-uniform Airy approximations are used and by extending the applicability of the method to body waves of the type *SmKS*.

We find, following the method of Richards (1973), that the required integral of horizontal displacement of *SmKS* for a point shear force in a radially varying but spherically symmetric earth is

$$u_H(r_s, \Delta_0, \omega) = \frac{L_s \exp(-i\pi/4)}{r r_s} \beta_s \left(\frac{\omega \beta_s}{2\pi\rho\beta \sin\Delta_0}\right)^{1/2} \int_\Gamma \left(\frac{p \cos j}{\cos j_s}\right)^{1/2} T_{SK} R_{KK}^{(m-1)} T_{KS} \times \exp(i\omega J)\, dp \qquad (1)$$

where ω is radian frequency; β is shear velocity; ρ is density; r is radius of receiver; a quantity with subscript s is evaluated at the source; p is complex ray parameter; $L_s = F/(4\pi\rho_s^{1/2}\beta_s^3)$ and $F\delta(\mathbf{r} - \mathbf{r}_s)H(t)$ is the potential whose gradient gives the equivalent body force of the source; and

$$\cos j_{(s)} = \left(1 - \frac{p^2\beta_{(s)}^2}{r_{(s)}^2}\right)^{1/2}.$$

The phase delay integral, J, is given by

$$J(r,p) = \int_{r_p}^{r_s} \left(\frac{\cos i}{v}\right) dr + \int_{r_p}^{r} \left(\frac{\cos i}{v}\right) dr + p\Delta_0 = T(r,p) - p\Delta(r,p) + p\Delta_0 \tag{2}$$

with $T(r,p)$, $\Delta(r,p)$, and $\cos i$ using the shear or compressional velocity, v, appropriate to *SmKS* at the radius r, and r_p is the radius of the turning point. Γ is a path in the complex ray parameter plane which crosses the real p axis at any convenient point on or near the saddle point of the WKBJ approximation. The quantities T_{SK}, R_{KK} and T_{KS} are the reflection/transmission coefficients at the core–mantle boundary,

$$\begin{aligned}
T_{SK} &= -4\rho_m \alpha_c \beta_m s \cos i_m \cos j_m / D \\
R_{KK} &= (D - 2\rho_c \cos i_m)/D \\
T_{KS} &= 4\rho_c \beta_m^2 s \cos i_c \cos i_m / D \\
D &= \rho_c \alpha_c \cos i_m + \rho_m \cos i_c (\alpha_m \cos^2 2j_m + 4\beta_m^3 s^2 \cos i_m \cos j_m)
\end{aligned} \tag{3}$$

where suffix m refers to the bottom of the mantle, c to the top of the core, α is compressional velocity, and the dependence on ray parameter is

$$\cos i_x = (1 - p^2 \alpha_x^2 / r^2)^{1/2} \qquad x = \mathrm{m}, \mathrm{c}$$

$$\cos j_m = (1 - p^2 \beta_m^2 / r^2)^{1/2}$$

$$\cos 2j_m = 1 - 2p^2 \beta_m^2 / r^2$$

$$s = p/r \quad \text{and} \quad r = r_m .$$

The vertical displacement of *SmKS* is obtained by inserting the factor $i\beta p/r \cos j_m$ in the integrand. To relate these theoretical amplitudes to recorded data requires accounting for the effect of the free surface of the earth. This entails essentially a doubling of *SV* amplitudes of core phases.

Equation (1) reduces to ray theory and geometric spreading if the assumptions are made that significant contributions arise only near the ray theory saddle point and if plane-wave reflection/transmission coefficients (equation (3)) are valid. These conditions are not valid when a ray has a turning point in the vicinity of a discontinuity. The path of integration must now be deformed to take into account the contribution of poles which arise from the zero of the denominator of the reflection/transmission coefficients at the core–mantle boundary. There are three systems of poles, one each arising from *P* and *S* waves grazing the mantle side of the core–mantle boundary, and one from a *P* wave grazing the underside of the core. Each system of poles strings along a line starting near, but not on, the real ray parameter values of core-grazing *P* and *S* rays (Fig. 1). For model 1066B of Gilbert & Dziewsonki (1975) these core-grazing values are at ray parameters 255.0, 481.3, and 437.5 s for, respectively, *P* and *S* incident from above and *P* incident from below the interface.

Furthermore, the reflection/transmission coefficients of ray theory are no longer adequate. Reflection/transmission coefficients commonly employ ratios of the radial wave function and its derivative in the form

$$C^{(j)} = \frac{v}{\pm i\omega} \frac{1}{g^{(j)}} \frac{\partial g^{(j)}}{\partial r} \qquad j = 1, 2 \tag{4}$$

where $g^{(j)}$ are the radial eigenfunctions satisfied by the wave equation (outgoing from the centre of the earth for $j = 1$ and ingoing for $j = 2$). Coefficients calculated using these ratios

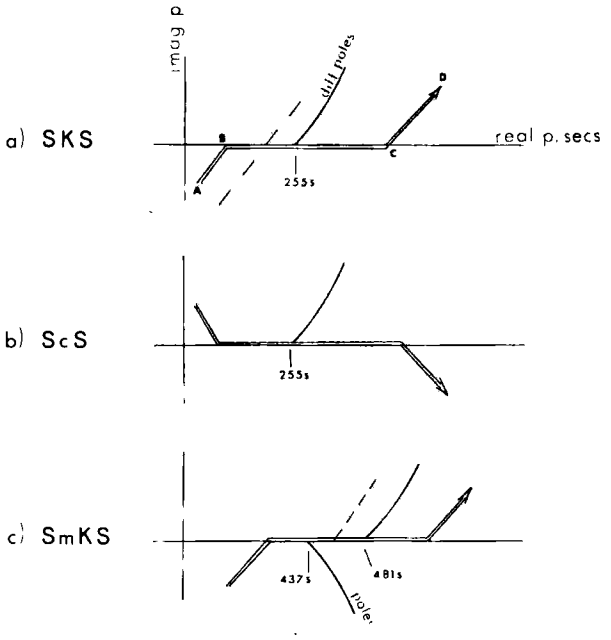

Figure 1. The complex ray parameter plane in units of s/rad (i.e. s). The diffraction poles string upwards for rays grazing the discontinuity from above (such as P(diff) and S(diff)), while the poles string downwards for rays grazing below (such as the ray which just grazes the underside of the core mantle boundary). For model 1066B, the core-grazing values are 255.0 s for P(diff), 481.3 s for S(diff) and 437.5 s for the P wave which grazes just within the core. (a) The path of integration for *SKS*. The dashed line shows the path of steepest descent used in ray theory. Typical values for the path *ABCD* are enumerated in Table 1. (b) The path of integration for *ScS*, a body wave without a turning point. (c) A typical path of integration for *SmKS*, $m \geqslant 2$. For high frequencies, the contributions to the integral become negligible long before the integration path reaches the diffraction poles near 481.3 s, so a shorter path (dashed line) can be used which shortens computation time.

are valid whether the turning point of a ray is near or remote from a discontinuity. Applying the WKBJ approximation to $g^{(j)}$ makes both $C^{(1)}$ and $C^{(2)}$ equal to the ordinary cosine of the angle of incidence. However, this is accurate only in cases where the turning point is far from a discontinuity. In the Langer approximation, the $g^{(j)}$ are approximated by

$$g^{(j)} = A_j \xi^{1/2} H_{1/3}^{(j)}(\omega\xi) \Big/ r\left(\frac{1}{v^2} \quad \frac{p^2}{r^2}\right)^{1/2} \tag{5}$$

where A_j are chosen so that $g^{(j)}$ reduces to a spherical Hankel function in the limit of a homogeneous medium; $H_{1/3}^{(j)}$ are Hankel functions; and

$$\xi = \int_{r_p}^{r} \left(\frac{1}{v^2} \quad \frac{p^2}{r^2}\right)^{1/2} dr$$

(v is the P or S velocity appropriate to radius r). Note that $\omega\xi$ is just the phase of the WKBJ approximation. Using this approximation, equation (4) becomes

$$C^{(j)} = \cos x \exp(\pm i\pi/6)\, H_{2/3}^{(j)}(\omega\xi)/H_{1/3}^{(j)}(\omega\xi) \tag{6}$$

where $\cos x = [1 - (p^2v^2/r^2)]^{1/2}$. In regions far from a turning point ($|\omega\xi|$ large), the coefficient of the cosine in equation (6) is practically unity, and thus, $C^{(1)} = C^{(2)} = \cos x$. However, in the region of the turning point, where $\cos x$ and $|\omega\xi|$ are near zero, $C^{(j)}$ remains finite. The $C^{(j)}$ of equation (6) are called generalized cosines, because of their quantitative dependence on frequency, on the radius of curvature, and on earth structure near the discontinuity. $C^{(1)}$ may be referred to as the upgoing cosine since it is defined by the upgoing radial wave functions, and $C^{(2)}$ is the downgoing cosine.

It is the values of equation (6) which are needed in the reflection/transmission coefficients, rather than $\cos x$. Implementation of the Langer approximation requires simply replacing the cosines in the reflection/transmission coefficients by the appropriate up/downgoing generalized cosines. Equations (3) become

$$\begin{aligned} T_{SK} &= [-2\rho_m \alpha_c \beta_m s C_i^1 (C_j^2 + C_j^1)]\ [h_m^2(r_m)/g_c^2(r_m)]/D \\ R_{KK} &= [-\rho_c \alpha_c C_i^1 + \rho_m C_k^1 (\alpha_m \cos^2 2j_m + 4\beta_m^3 s^2 C_i^1 C_j^1)]\ [g_c^1(r_m)/g_c^2(r_m)]/D \\ T_{KS} &= [2\rho_c \beta_m^2 s (C_k^2 + C_k^1) C_i^1]\ [g_c^1(r_m)/h_m^1(r_m)]/D \\ D &= \rho_c \alpha_c C_i^1 + \rho_m C_k^2 (\alpha_m \cos^2 2j_m + 4\beta_m^3 s^2 C_i^1 C_j^1) \end{aligned} \tag{7}$$

where subscript i is for mantle P waves, j is for mantle S waves, and k is for core P waves and parentheses about the superscripts of C, h, and g are understood. The h's (g's) are radial wave functions using $S(P)$ velocities; subscripts m and c indicate which velocities, mantle or core, are used. The ratios of radial wave functions (such as $g_c^{(1)}/g_c^{(2)}$) are needed to account for the phase between the depth of the turning point of the ray and the depth of the core mantle boundary. Since the Langer and WKBJ approximations merge at large $|\omega\xi|$, computation time can be considerably shortened by choosing a value of $|\omega\xi|$ beyond which the usual phase and cosines of the WKBJ method are computed rather than the more rigorous combination of Hankel functions. In the subsequent calculations, a satisfactory criterion was chosen at $|\omega\xi| > 5$.

The total transmission coefficient relevant to the body-wave SKS is $T_{SK}T_{KS}$, which is plotted in Fig. 2 as a function of real ray parameter. The curves of ray theory and two other frequencies (0.03125 and 0.125 Hz) illustrate the extent of frequency dependence.

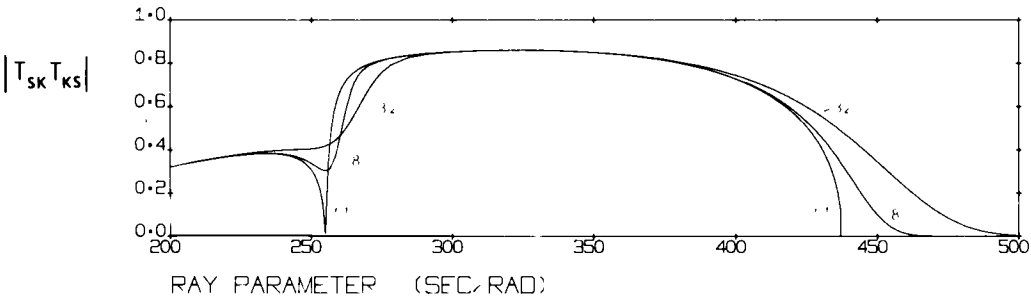

Figure 2. The amplitude of the combined transmission coefficient $T_{SK}T_{KS}$ as a function of real ray parameter. T_{SK} is the transmission coefficient for an S wave in the mantle which is refracted into the core as a P wave, and T_{SK} describes the mode-conversion of a P wave in the core which is refracted into the mantle as an S wave. Real ray parameter is related to the angle of incidence at the core mantle boundary by $p = (r_m \sin i_m)/\beta_m$. Curves are shown for 0.03125 Hz (32 s), 0.0125 Hz (8 s) and for ray theory. The curves of the finite frequencies do not behave as discontinuously as ray theory would predict. This coefficient describes $SmKS$ as well, since its relevant transmission coefficient may be written as $(T_{SK}T_{KS})R_{KK}^{m-1}$. R_{KK} is described in detail by Richards (1976), and it also exhibits the type of frequency dependence seen in this figure.

The transmission coefficient of ray theory is zero at two ray parameters, 255.0 and 437.5 s. When *SKS* interacts with the core–mantle boundary, a *P* wave in the mantle may arise from the mode-conversion of *S* incident on the core or by the transmission of *P* out of the core. The mantle *P* with the ray parameter of 255.0 s just grazes the core. Its decay at the boundary is what, according to ray theory, cause the abrupt zero in the transmission coefficient. For finite frequencies, however, the coefficients show a continuous transition across the critical ray parameter, and curves of the lower frequencies tend to be smoother. A similar phenomenon occurs at the ray parameter near 437.5 s. At this value, the refracted *P* entering the core grazes the underside of the core–mantle boundary. For ray parameters exceeding this critical value, *P* cannot possibly, according to ray theory, be refracted into the core and incident *S* is instead totally reflected at the boundary. However, for finite frequencies, the transmission coefficient for ray parameters beyond critical decays smoothly. In addition, very small amounts of energy are transmitted even beyond the critical value for diffracted *S* ($p = 481.3$ s). The neglect of the frequency dependence shown here can lead to some gross misinterpretations of the core–mantle boundary, which will be discussed in more detail when *SKS* is examined below.

3 Time-domain solution

Up to this point, the displacement components have been calculated as a function of frequency in the form

$$u(\Delta_0, \omega) = \int_\Gamma \omega^{1/2} f(p, \Delta_0) \exp(i\omega J)\, (p, \Delta_0)\, dp \tag{8}$$

for $\omega \geq 0$. The inversion to the time-domain solution is readily obtained from

$$u(\Delta_0, t) = \frac{1}{\pi} \int_0^\infty \omega^{1/2} \operatorname{Re}\left\{ \int_\Gamma f \exp(i\omega J)\, dp \exp(-i\omega t) \right\} d\omega \tag{9}$$

Since the path Γ need pass only approximately over the saddle point of ray theory associated with a given distance, a substantial reduction in computation time is achieved by using the same integration path for a suite of distances, in which case f and J are easily modified for each distance. In contrast, Cagniard methods require an exact saddle point path of integration and a separate path and recalculation is required for every distance. Typical integration paths for some long-period body waves, and the distances over which they are applicable are given in Table 1. The density (number and spacing) of points required for numerical integration is determined by how well the integrand behaves. The integrand is smoother for lower frequencies and for the portion of the path which decays.

In practice, the amplitude and phase spectra of *SmKS* ($m \geq 2$) are adequately defined by computing displacements of as few as 20 equally spaced frequencies for a Nyquist frequency of 0.5 Hz (e.g. Fig. 16). The spectra of *SKS* is more complicated than that of *SmKS* (e.g. compare Figs 9 and 16), but 32 frequencies sufficiently define its spectra. Additional frequency components, other than those explicitly calculated, are obtainable by linear interpolation of amplitude and phase. There are, of course, discontinuous jumps in the phase spectra from π to $+\pi$ which is a consequence of the trigonometric algorithms employed by the computer. The ambiguity of $2k\pi$ (k an integer) in the computed phase may be resolved by using the travel-time of ray theory (see Appendix). The time-domain solution is conveniently obtained by a fast Fourier transform of 2^n frequency components (n an integer). The time series must be sufficiently long to avoid complications inherent in the

Table 1. Typical integration paths in the complex ray parameter plane for some body waves. They are applicable for distances between 100° and 125°. Because the contributions to the integrand decay much quicker for higher frequencies, two paths are given for each body wave. The first one applies to frequencies between 0.015625 and 0.265625 Hz. The second one is a shorter path (which saves computation time) and applies to frequencies between 0.28125 and 0.5 Hz. The number outside the parentheses refers to the subdivisions of a path needed for the numerical integration. Our units for ray parameter are s/rad – a natural choice for evaluation of $r \sin i/v$.

	AB	*BC*	*CD*
SKS	(100, −70), (170, 0), 31	(170, 0), (260, 0), 62	(260, 0), (360, 100), 51
	(140, −25), (170, 0), 31	(170, 0), (260, 0), 123	(260, 0), (310, 50), 56
SKKS	(298, −50), (358, 0), 51	(358, 0), (482, 0), 61	(482, 0), (508,100), 51
	(338, −30), (358, 0), 21	(358, 0), (408, 0), 82	(408, 0), (428, 100), 21
SmKS	(325, −50), (400, 0), 21	(400, 0), (505, 0), 72	(505, 0), (575, 70), 15
	(380, −5), (400, 0), 21	(400, 0), (425, 0), 51	(425, 0), (470, 70), 45

cyclic nature of the Fourier transform. The results in the subsequent sections of this paper require no more than 64 frequency components which give a time signal of length 128 s for a sampling rate of 1 s. In a following section, the body waves *SKS*, *SKKS* and the entire sum of *SmKS* ($m = 3 \ldots, M$; where M truncates the series and is a value to be determined) are synthesized separately. The total theoretical seismogram is the sum, with the appropriate time delays given by ray theory, of each body-wave displacement. The run which consumes the most computation time, that of calculating the amplitude and phase of 32 frequency components of *SKS* for 10 distances, uses no more than 2.60 min on an IBM 360/95. The time to compute the total seismograms for 10 distances, in which M was taken up to 15, is about 7.0 min for model 1066B.

In order to compare theoretical and actual seismograms, the displacement $u(t, \Delta_0)$ must be convolved with the instrument response (I), the finiteness of source duration (D), the crustal response at the source and receiver (C), the attenuation along the propagation path (A), and multiplied by the source radiation pattern (S). Then the resulting seismogram, $U(t, \Delta_0)$, is

$$U(t, \Delta_0) = u(t, \Delta_0) * I * D * C * A \times S. \tag{10}$$

For instrument correction, a rational bi-linear z transform obtained from the equations of Hagiwara (1958) for an electromagnetic seismograph is convolved with the displacement time signal. For attenuation, one can easily allow the velocity profile of a given earth model to have an imaginary part, since the ray parameter is already a complex quantity in this development of the full wave theory (Cormier & Richards 1976). There was no need to do this, however, for the synthetic seismograms of *SmKS* that are shown below agree very well with actual records even if anelasticity is neglected. This observation is in accord with that of Müller (1973) in which attenuation was also found either unimportant or at least not a sensitive property for the long-period *PKP* body waves.

To account for the source radiation pattern in the displacement, the results of Ben-Menahem, Smith & Teng (1965) may be used. For a point source with double couple faulting in a homogeneous earth, the radiated displacement for *SV* waves is described by

$$u_{sv}(\mathbf{r}, \omega) = F_s A_\phi \frac{\exp(i\omega T)}{R} \hat{\phi} \tag{11}$$

where

$$F_s = \frac{M_0}{4\pi\rho_s\beta_s^3}, \quad M_0 = \text{moment}, \quad R = |\mathbf{r} - \mathbf{r}_s|, \quad \text{and} \quad A_\phi = (\mathbf{n}\cdot\hat{\mathbf{R}})(\mathbf{a}\cdot\hat{\phi}) + (\mathbf{a}\cdot\hat{\mathbf{R}})(\mathbf{n}\cdot\hat{\phi}).$$

The quantities defining A_ϕ are

a = unit vector in the direction of displacement

$\hat{\mathbf{R}}$ = unit vector along the ray

$\hat{\phi}$ = unit vector normal to the direction along the ray but in the plane of propagation (*SV* motion)

n = unit vector normal to the fault plane.

The displacement of equation (11) must be generalized to an inhomogeneous (radially varying but spherically symmetric) earth. The object is to introduce the factor A_ϕ correctly into the displacement integral of equation (1). The modified displacement requires a normalization such that in the limit of ray theory it describes geometric spreading. For a homogeneous earth, geometric spreading and phase delay is described by $\exp(i\omega T)/R$. For a radially varying earth, T is easily changed to $T(\mathbf{r}, \mathbf{r}_s)$ by computing the appropriate travel time between the radius at the source, r_s, and the radius at any point along the ray, r. In order to generalize R to $R(\mathbf{r}, \mathbf{r}_s)$ for a radially varying earth, consider the following quantity

$$G = \exp(-i\pi/4)\frac{1}{rr_s}\left(\frac{\omega}{2\pi \sin\Delta_0}\right)^{1/2}\int_\Gamma \sqrt{\frac{p}{\cos j \cos j_s}}\,\exp[i\omega J(r,p)]\,dp. \tag{12}$$

In the limit of ray theory, G is evaluated at the saddle point, p_0. For $d\Delta/dp < 0$,

$$G = \frac{\exp[+i\omega T(\mathbf{r}, \mathbf{r}_s)]}{rr_s}\left\{\frac{\sin\Delta_0}{p_0}\cos j \cos j_s\left(\frac{-\partial\Delta}{\partial p}\right)\right\}^{-1/2}.$$

But Richards (1971, p. 463) identifies this form of G as exactly the geometrical spreading factor $1/[\beta_s R(\mathbf{r}, \mathbf{r}_s)]$. Also, $|u(\mathbf{r}, \omega)| \propto 1/[R(\mathbf{r}, \mathbf{r}_s)\sqrt{\rho\beta}]$, which is a condition that conserves flux of energy across the area of a ray tube (Bullen 1963), so we redefine F_s for a radially varying earth as $M_0/[4\pi\sqrt{\rho\rho_s}\beta\beta_s^{5/2}]$. Thus, the displacement in equation (10) can now be written as

$$u_{sv}(\mathbf{r}, \omega) = \frac{M_0}{4\pi\sqrt{\rho\rho_s\beta}\,\beta_s^{5/2}} A_\phi\hat{\phi}\exp(-i\pi/4)\left(\frac{\beta_s}{rr_s}\right)\left(\frac{\omega}{2\pi\sin\Delta_0}\right)^{1/2}\int_\Gamma\left(\frac{p}{\cos j\cos j_s}\right)^{1/2}\exp(i\omega J)\,dp. \tag{13a}$$

Comparing this with equation (1), (omitting reflection/transmission coefficients), it is seen that

$$L_s = \frac{M_0}{4\pi}\,\frac{A_\phi}{\sqrt{\rho_s}\beta_s^3\cos j}.$$

In a similar fashion, it may be shown that

$$u_p = L_p' A_R\,\hat{\mathbf{R}}\,\frac{\exp(\,i\pi/4)\alpha_s}{rr_s}\left(\frac{\omega}{2\pi\sin\Delta_0}\right)^{1/2}\int_\Gamma\left(\frac{p}{\cos i\cos i_s}\right)^{1/2}\exp(i\omega J)\,dp \tag{13b}$$

$$u_{sh} = L_s' A_\theta\,\hat{\theta}\,\frac{\exp(-i\pi/4)\beta_s}{rr_s}\left(\frac{\omega}{2\pi\sin\Delta_0}\right)^{1/2}\int_\Gamma\left(\frac{p}{\cos j\cos j_s}\right)^{1/2}\exp(i\omega J)\,dp \tag{13c}$$

where $L_s' = M_0/[4\pi\sqrt{\rho_s\rho\beta}\,\beta_s^{5/2}]$ and $L_p' = M_0/[4\pi\sqrt{\rho_s\rho\alpha}\,\alpha_s^{5/2}]$, $A_R = (\mathbf{a}\cdot\hat{\mathbf{R}})(\hat{\mathbf{n}}\cdot\hat{\mathbf{R}})$, $A_\theta = (\mathbf{n}\cdot\hat{\mathbf{R}})(\mathbf{a}\cdot\hat{\theta}) + (\mathbf{a}\cdot\hat{\mathbf{R}})(\mathbf{n}\cdot\hat{\theta})$, $\hat{\theta}$ = unit vector perpendicular to the plane of propagation of the ray (*SH* motion).

The angles in p, $\cos j_{(s)}$, $\cos i_{(s)}$, A_R, A_θ and A_ϕ are based on the angle defined by the saddle point ray parameter. If any of the quantities are strongly dependent on ray parameter they should be put inside the integral. The sensitive reflection/transmission coefficients, for instance, would be inside the integral if they are needed.

For large enough earthquakes, the correction for finite source duration (also called the directivity correction) is required. It simulates the directional distribution of apparent pulse widths which results from the time history of the fault rupture. For a rectangular fault with a unilateral propagating ramp dislocation in time, the associated effect of finiteness is equivalent to convolving the time-domain displacement with a unit area box-car of duration equal to the sum of the rise time and apparent rupture time (Haskell 1964). The mechanism for deep earthquakes is still not well understood. Nevertheless, there are many lines of evidence to indicate that deep earthquakes behave as double-couple sources (e.g. Mikumo 1969; Fukao 1970; Billington & Isacks 1975). Thus, the directivity correction is also appropriate for the deep earthquakes that are studied in this paper. If the mechanism of deep earthquakes is one of a sudden change (say, in shear modulus as proposed by Knopoff & Randall 1970) which occurs throughout a fault volume, as opposed to a rupture propagating from a region of nucleation, the convolution with a box-car is still valid. The duration of the box-car would then be comprised of a rise time and an apparent rupture time which may not be as sensitive to azimuth as would be the case for unilateral rupture. In practice, convolving long-period seismograms with a box-car of greater than 7 s duration produces discontinuities in the synthetic records and a dislocation model with a smoother source function should be employed. None of the synthesized seismograms in this paper required a box-car of more than 5 s. The pulse width of long-period body waves is so sensitive to the directivity correction that the uncertainty in having chosen the correct duration is not more than 1 s for durations up to 10 s.

Moments may be assigned if the absolute amplitudes of synthetic and actual waveforms can be matched. However, since equation (13) cannot be used directly if the synthetic has been convolved with a box-car, we must now derive the required expression. Following Haskell (1964), we describe the far-field elastic displacement of an SV wave for a planar fault service, Σ, as

$$u(\mathbf{r}, t) = [1/(4\pi\sqrt{\rho\rho_s\beta}\,\beta_s^{5/2})]\; G \iint \mu\,[\dot{u}(t - T(\mathbf{r},\boldsymbol{\xi})]\; d\Sigma \tag{14}$$

where $[u]$ is the displacement discontinuity, $\boldsymbol{\xi} = (\xi_1, \xi_2)$ are coordinates on the fault plane, and

$$G = A_\phi \exp(-i\pi/4)\left(\frac{\beta_s}{rr_s}\right)\left(\frac{\omega}{2\pi \sin\Delta_0}\right)^{1/2} \int \left(\frac{p}{\cos j \cos j_s}\right)^{1/2} \exp(i\omega J)\, dp.$$

G can incorporate reflection/transmission coefficients if needed. Using

$$T(\mathbf{r}, \boldsymbol{\xi}) = T(\mathbf{r}, 0) - T(0, \boldsymbol{\xi}) = T_0 - \xi\cos\theta/\beta_s,$$

equation (14) transforms to the frequency domain as

$$u(\mathbf{r}, \omega) = [1/(4\pi\sqrt{\rho\rho_s\beta}\,\beta_s^{5/2})]\; G \exp(i\omega T_0) \iint \mu \exp(-i\omega\xi)\,(\cos\theta/\beta_s)\,[\dot{u}(\xi, \omega)]\; d\Sigma \tag{15}$$

where θ is the angle between $\boldsymbol{\xi}$ and the ray. For an unilaterally propagating step model, $[u(\mathbf{r}, t)] = dH(t - \xi/c)$ and $[\dot{u}(\xi, t)] = d\delta(t - \xi/c)$, where c is the rupture velocity and d is

the dislocation. Inserting these expressions into equation (5), we obtain

$$u(\mathbf{r}, \omega) = [(\mu G \exp(i\omega T_0)/(4\pi\sqrt{\rho\rho_s\beta}\,\beta_s^{5/2})]\, dW \int_{-L/2}^{L/2} \exp[i\omega\xi_1(1/c - \cos\theta/\beta_s)]\, d\xi_1 \qquad (16)$$

$$= [(G \exp(i\omega T_0)/(4\pi\sqrt{\rho\rho_s\beta}\,\beta_s^{5/2})] \left[M_0 \frac{\sin x}{x}\right]$$

where W is fault width, L is fault length, $X = \omega L/2(1/c - \cos\theta/\beta_s)$ and $M_0 = \mu LWd$. Transforming to the time domain we have

$$u(\mathbf{r}, t) = [1/(4\pi\sqrt{\rho\rho_s\beta}\,\beta_s^{5/2})]\, GM_0 * B(t) \qquad (17)$$

where $B(t)$ is a box-car of unit area having duration $L(1/c - \cos\theta/\beta_s)$.

Table 2. Seismograms from two deep earthquakes that are used in this study. Focal mechanism solutions were determined by the author. The nearly vertical nodal plane is very well constrained, but the more horizontal nodal plane is not well constrained.

	Origin time		Location	Depth	m_b	Pole of nodal planes	
Fiji	1971 November 20	07 28 01.0	23.4S 179.9W	551 km	6.0	240, 10	190, 74
S. Fiji	1973 July 21	04 19 17.1	24.8S 179.2W	411 km	5.9	315, 10	225, 60

By using deep earthquakes (Table 2) in this study, crustal corrections for long-period theoretical seismograms need be considered only for the receiver end of the propagation path. Furthermore, the nature of the body waves under study helps to minimize the complexities of the crustal response. We note that only the horizontal (radial) seismogram and its associated crustal response are synthesized throughout this paper because the limiting ray parameter for all *SmKS* is 437.5 s. The effect of this limit is to restrict the deviation from vertical of the angle of incidence at the base of the crust to no more than 14° for all *SmKS* rays. Thus, shear-wave energy is recorded almost entirely on the horizontal-component seismograph. The near vertical angle of incidence of *SmKS* also insures that the amount of mode-converted *P* energy is slight, and whatever amount that is produced will arrive predominantly on the vertical, rather than the horizontal, component seismograph. Thus, it is not surprising to find that all the reverberations of the horizontal response for various crustal models can always be associated, on the basis of arrival times, with the primary multiple reflection of an *S* wave from a first-order discontinuity, e.g. Fig. 3(a).

The crustal correction can easily be made with the matrix method of Haskell (1962). But it is necessary only if the signatures of the synthetic body waves are significantly altered by

Table 3. Crustal models that are used in Fig. 3 for testing the effect of crustal response. Crust 1 is taken from Dorman & Ewing (1962) and appears to be the best model for the crust under OGD. The impedance is calculated with shear velocities.

Crustal model	Layer No.	α (km/s)	β (km/s)	ρ (g/cm^3)	Thickness (km)	Impedance
1	1	6.15	3.64	2.86	38	0.19
	2	8.14	4.69	3.30	∞	
2	1	4.69	2.58	2.18	15	0.23
	2	6.15	3.64	2.86	18	0.19
	3	8.14	4.69	3.30	∞	

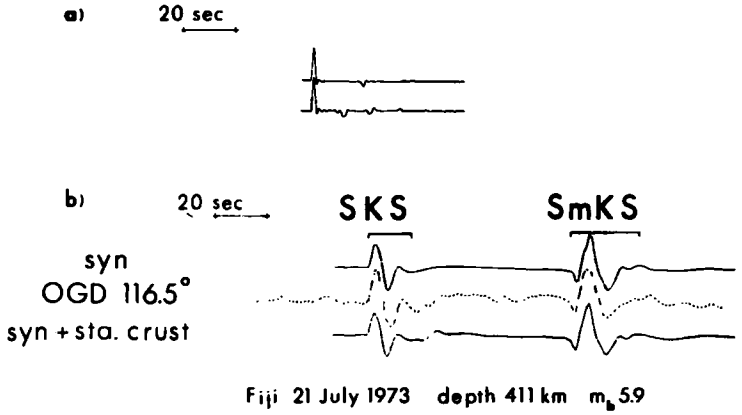

Figure 3. (a) Top: Horizontal component of the crustal response for a homogeneous crust over a mantle half-space (crust 1, Table 3). Bottom: Horizontal component of the crustal response for a two-layered crust over a mantle half-space (crust 2, Table 3). (b) Top: Synthetic seismogram of the horizontal displacement of *SKS* and *SmKS* ($m \geqslant 2$) at a distance 116.5° and source depth 411 km. Brackets above the record delimit the portion of the waveform which must correlate with the observed data. Middle: Observed EW seismogram from OGD for the Fiji earthquake of 1973 July 21. Bottom: The synthetic seismogram of the top record convolved with the crustal response of a homogeneous layer over a half-space (crust 1, Table 3).

the structure beneath a station. By synthesizing numerous seismograms for different crusts and different earth models, Choy (1976) demonstrated that crustal effects were, indeed, minor for long-period *SmKS*. One of his examples, shown in Fig. 3(b), simulates the effect of the crust under OGD which consists of a homogeneous layer over a mantle half-space. Inserting the crustal response no doubt enhances the appearance of the synthetic seismogram, but it serves only to distract one's attention from the significant characteristics of the earlier part of the body wave. It was found that only when the crust contained at least one discontinuity, other than the crust–mantle interface, with an impedance jump greater than about 25 per cent in shear velocity would the resulting reverberation have sufficient amplitude to modulate the coda of the main body wave. Even in this extreme case crustal reverberations were easily identifiable. There was little difficulty in relating the characteristics of the actual body wave to a synthetic waveform computed without a crustal response. Consequently, since our aim is to study the isolated waveforms of *SKS* and *SmKS*, as opposed to studying crustal structure, we need not apply a crustal correction to synthetic records presented in later sections of this paper.

4 Properties of *SmKS*

We begin this section by demonstrating the importance of *SmKS* data in constraining earth models. Then it is shown that conventional measurements of arrival or differential travel times of *SmKS* are difficult if not impossible to obtain. Finally, we describe how the integration paths of *ScS*, *SKS*, *SKKS*, and *SmKS* are chosen.

In determining the velocity profile for the upper few hundred kilometres of the outer core, *SmKS* body waves are more useful than *PmKP* body waves. Body waves of the type *PmKP* encounter a discontinuous velocity decrease at the core–mantle boundary, which results in a shadow zone in surface observations. On the other hand, when *S* in the mantle is transmitted into the core as *P*, it encounters a velocity increase which refracts the wave upwards. So *SmKS* has no shadow zone in the core. This fact accounts for the statement

by Wiggins *et al.* (1973) that the differential times of *SKS–SKKS* are much more influential than *PmKP* in constraining the permissible velocity profiles in the outer core for a given earth model. But the statement pertains only to the set of data consisting of *useful* travel times. Useful travel times are available at those distances where *SKS* is clearly separable from *SKKS*. This distance would be about 100° for deep earthquakes ($h \geqslant 400$ km) and 110° for shallow ones. (With shallow earthquakes, in contrast to deep ones, *sSKS* interferes with *SKKS* till about 110°, more or less, depending on depth.) Thus, there is still a portion of the outer core which is not constrained by *SKS–SKKS* data. Another complication is that all body waves of the family *SmKS* except for *SKS* are non-minimum travel-time paths. In propagating through the Earth, these *SmKS* touch a number of internal caustics which may produce a severely distorted waveform compared to that which originally was radiated from the source (Jeffreys & Lapwood 1957; Hill 1974; Choy & Richards 1975). Thus it turns out that *SKKS* travel times, such as those presented by Hales & Roberts (1971), may not be useful after all unless the seismograms are corrected for phase distortion with methods like those suggested by Choy & Richards (1975) or Clayton, McClary & Wiggins (1976).

It might be asked why one does not use the travel times of *S3KS*, *S4KS* and so on. Fig. 4 depicts the propagation paths of some *SmKS*. For distances less than 125°, the turning point of the body wave *S3KS* is in the upper 200-km of the outer core. The turning point of the

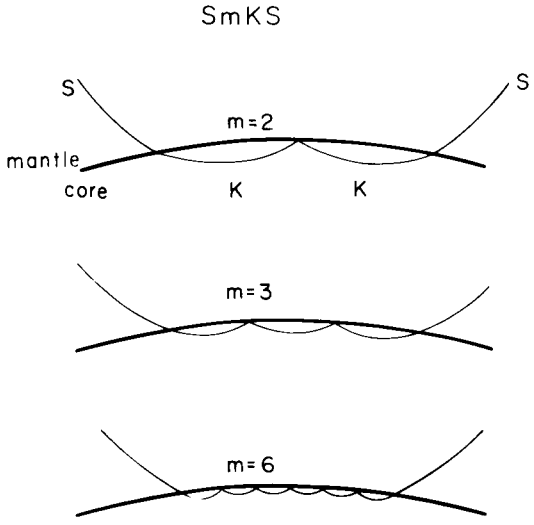

Figure 4. Typical propagation paths of *SmKS* for $m = 2$, 3 and 6. A discontinuous velocity increase across the core mantle boundary refracts the rays which enter the core upwards. As the order of the multiple reflection, m, increases, one can see that the propagation paths differ less and less. Thus, as the order of the multiple increases the ray parameters and travel time of *SmKS* converge to a limit.

next higher multiple, *S4KS*, is in roughly the upper 75-km of the outer core. With each higher multiple, the rays bottom shallower and shallower in the core. There would be a wealth of data on the outer core if *SmKS* travel-time data were available. Unfortunately, as one may imagine from Fig. 4, as the order of the multiple increases, the propagation paths and travel times converge to a limit. Fig. 5 shows this effect on the travel-time curves. The seismogram is complicated in that the arrival times of each successively higher order reflection is within the coda of previous lower order reflections. For deep earthquakes ($h \geqslant 400$ km) *SKKS* does not clearly separate from *SKS* till beyond 100°. It is not till beyond 125° that

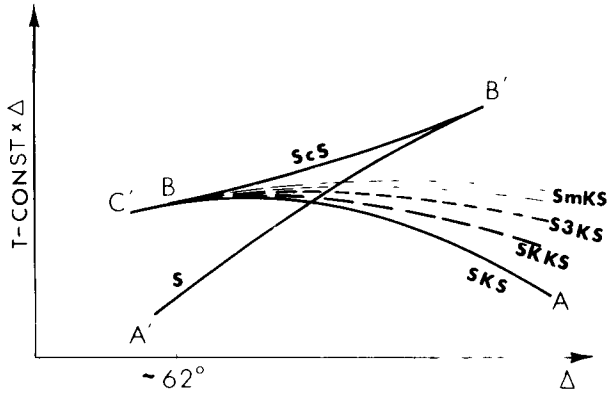

Figure 5. The configuration of $T-\Delta$ curves for SV waves in the earth. B is the cusp of the AB branch of all *SmKS* and is located at about 62°. The DF branch of *SKS* (called *SKIKS*) encounters the inner core and is not shown. The triplication and the infinite number of transmitted rays are a characteristic feature of the family of rays which arises from any discontinuous velocity increase.

S3KS becomes visually separable from *SKKS*. The arrival times of the high-order reflections are nearly impossible to pick because the waveforms all overlap.

To synthesize an adequate seismogram, it is essential to consider how and where all the body waves *SmKS* arise. We now describe the system of $T-\Delta$ curves for SV waves incident at the core in greater detail (Fig. 5). The forward branch of direct S, $A'B'$, is formed as real ray parameter decreases from its maximum value of 1873.8 s (for a surface focus in model 1066B) to the core-grazing value, 481.3 s. The critical ray parameter where P is diffracted along the underside of the core–mantle boundary is 437.5 s. S waves incident on the core with ray parameters between 481.3 and 437.5 s find that mode-converted P wave rays cannot penetrate the core. Instead, incident S is totally reflected to form a receding branch of *ScS*, BB'. For ray parameters less than 437.5 s, incident S is partitioned into *ScS* (BC') and the AB branch of an infinite number of *SmKS* rays. The cusp B is where *SmKS* rays first penetrate the core and is common to all *SmKS*. Only at distances far from the cusp do the differences in travel time of the AB branches of *SmKS* increase to the extent that the lower order reflections become separable from the chain of *SmKS* arrivals.

For distances at and beyond the cusp distance, the total seismogram is the sum of an infinite number of multiply reflected core phases, as well as *ScS*. For the mth multiple reflection, each body-wave displacement has in the integrand of equation (1) a factor of the form $T_{SK}R_{KK}^{m-1}T_{KS}$. Thus, the summation of *SmKS* displacements ($m = 1, \ldots, \infty$) forms a geometric series, often called the Debye series. This summation is rapidly convergent for rays which go from a medium of high velocity to one of low velocity (Nussenzweig 1969). But in the case of *SmKS*, the rays encounter a velocity increase on entering the core. Near the cusp in the region of total reflection of SV, the series is so slow to converge that it is computationally uneconomical. A further complication is that near a cusp the saddle points on the real p axis for reflected, transmitted and diffracted rays start to coalesce. An integration path must be chosen to include the proper poles for each type of ray. For rays scattered by a transparent sphere, Nussenzweig (1969) concluded that the path of integration for totally reflected S waves should account for residues of poles in the lower half of the p plane. In Fig. 1(b) and (c), these poles would be the ones emanating downards from $p = 437.5$ s. Ludwig (1970) and Uberall (1975) criticized these poles as being unphysical because their contributions increase exponentially as radius from the core–mantle boundary decreases. Indeed, we find that enclosing such poles in the integration path does result in ill-behaved

amplitudes for those *ScS* whose saddle point ray parameters are near or beyond the cusp value. The integration paths that we choose later do not require crossing or enclosing any portion of the line of poles in the lower half plane. Cormier & Richards (in preparation) have recently shown how to evaluate the total effect of multiples even near the cusp *B*, and have applied this theory to interpret a similar problem involving the multiples *PKmIKP*, i.e. of rays associated with the inner core–outer core boundary.

The calculations in this paper concentrate on the distance range in which *SKS* and *SKKS* have been most studied, between 100° and 125°. The reason for the lower bound is that, although *SKS* finally arrives earlier than *S* at 85°, it is not clearly separated from *SKKS* till 100°. Beyond 130°, the *DF* branch belonging to *SKIKS* precedes the *AB* branch of *SKS*. The upper bound of our computations is chosen to be 125°, to insure that the amplitudes of *SKIKS* and *SKiKS* are negligible. They arrive after *SKS* in this distance range, and their amplitudes are in fact on the order of one-twentieth that of *SKS*. Also, in this distance range, which is far from the cusp (about 62° for shallow earthquakes), the Debye series converges within a few terms. We shall show below that an adequate seismogram can be obtained by summing only the first 15 multiple reflections.

The saddle points of *SKS* between 100° and 125° do not exceed 280 s. The contributions to the integrand of equation (1) decay long before the integration path comes near the critical ray parameter of 437.5 s, and *SKS* is, in effect, a body wave separated in time from the other *SmKS* arrivals. An appropriate path of integration, Fig. 1(a), meets the real *p* axis at roughly an angle of 45°, as shown by Richards (1973) for rays which have turning points. Note that this is not the steepest descent path of ray theory – Fig. 1(a), dashed line – but is deformed to take account of the diffraction poles emanating from the saddle point of the core-grazing *P* wave.

The saddle points of *SKKS* between 100° and 125° range from 408 to 360 s. The path of integration, Fig. 1(c), is deformed to take account of diffraction poles emanating from the saddle point of the core-grazing *S* wave. The poles at 255 s are too remote to affect the displacement of *SKKS*. Note that this path does not enclose poles in the lower half *p* plane.

The saddle points of higher order *SmKS* are all between 417 and 437.5 s. As with *SKKS*, the path of integration detours around the poles in the lower half plane but it does enclose the poles associated with the core-grazing *S* wave. Because the saddle points are all squeezed into a small portion of the real *p* axis, computer time is optimized by using the same integration path for each multiple with only minor modifications in *f* and *J* of equation (15). These modifications involve raising the exponent of the internal reflection coefficient, R_{KK}, to the proper order, and accounting for the slightly different phase in *J*. It is more convenient to sum the body waves in the frequency domain than the time domain

$$\sum_{m=3}^{M} u(\Delta_0, t) = \frac{1}{\pi}\int_0^\infty \omega^{1/2}\,\mathrm{Re}\left\{\int_\Gamma \sum_{m=2}^{M} F(p, \Delta_0, m)\exp\left[i\omega J(p, \Delta_0, m)\right] dp \exp(-i\omega t)\right\} d\omega \tag{18}$$

where *M* is the cutoff in the Debye series where sufficient convergence is attained.

Our computations of *ScS* are in the distance range 20° - 50°. The saddle points on the real *p* axis range from 175 to 400 s. An appropriate integration path for *ScS* is oriented roughly −45° with respect to the real *p* axis, Fig. 1(b), as shown by Richards (1973) for rays without a turning point. The path is deformed to enclose poles arising near the ray parameter for core-grazing *P* waves, and the integrand decays well before coming near the poles in the lower half *p* plane. Integration paths for *ScS* at distances near and beyond the cusp distance (where real $p \geqslant 437.5$ s) cannot avoid these poles. Though *ScS* in these regions is not computed in this paper, integration paths and wave functions described by Ludwig (1970) and

Cormier & Richards (1977) are capable of resolving the problem by allowing rays entering the core near the critical angle of incidence (and whose internal reflections have turning points just barely within the core) to have a refracted component not only downwards, but upwards. This modification of the full wave theory removes the poles in the lower half p plane and introduces Regge poles in the upper half plane, whose residues account for whispering gallery modes.

5 Application to core phases

The emphasis of this section is on generating waveforms of long period body waves because frequency-dependent behaviour should be more pronounced in the long-period rather than short-period band. At the same time, long-period body waves are not as sensitive to small structures in the crust and upper mantle. Their wavelengths are sufficiently large that the assumption of a spherically symmetric earth may be justified. Because the *SmKS* have a steep angle of incidence at the surface of the earth (not exceeding 14° due to a limiting ray parameter of 437.5 s) almost all the entire shear displacement is horizontal. Consequently, only the horizontal radial components of displacement are synthesized.

Table 2 lists the parameters of two deep earthquakes from which seismograms recorded at WWSSN stations are chosen as a standard by which to judge the theoretical seismograms. Deep events are preferred for two reasons. First, the complications of crustal and upper mantle transfer functions at the source are greatly minimized. Second, the body waves *SKS* and *SKKS* are free of their surface reflected analogues, *sSKS* and *sSKKS*. In general, a source depth close to the depth of the events being studied should be used in the computations. Calculating body waves for a surface focus and then 'correcting' for depth by simply reducing the angular distance traversed by a ray may yield correct travel times, but the $p-\Delta$ systematics may yield different amplitudes.

In this section the earth model 1066B is used to illustrate the features of theoretical seismograms. In the following section, where the sensitivity of *SmKS* to properties of the outer core is examined, 1066B is employed only as a starting model.

5.1 *SKS* AND *SP*(DIFF)*KS*

Between 100° and 125°, the saddle points of *SKS* on the real p axis range from 280 to 175 s. An appropriate path of integration, shown in Fig. 1(a), is deformed to take account of the line of diffraction poles which emanate from the ray parameter of the core-grazing P wave ($p = 255$ s). The contribution of the residues thus included in the integration is not insignificant, and corresponds to P energy diffracted at the core–mantle interface which eventually travels through the core and is then refracted upwards in the mantle as S. The total body wave represented in the calculation is the combination of *SKS* and what may be called *SP*(diff)*KS*. The existence of *SP*(diff)*KS* has been noted before by Kind & Müller (1975) when synthesizing *SV* body waves by the reflectivity method. However, the reflectivity method returns a multitude of reverberations from which the *SP*(diff)*KS* is an inferred arrival. The full wave theory, on the other hand, gives the advantage of actually seeing how a physical entity, *SP*(diff)*KS*, is directly related to the mathematical concept of diffraction poles. Fig. 6 (top) attempts to illustrate a ray picture of these body waves. Two paths of *SP*(diff)*KS* are depicted in order to emphasize that an infinite number of such paths connect source and station. These paths travel partly as a P wave in the core and partly as a diffracted wave. All these possible paths have in common that the angular distance traversed by *P*(diff)*K* is constant. The $p-\Delta$ relationship of *SKS* to *SP*(diff)*KS*, Fig. 7(a), shows that the latter is always a later arrival than *SKS*.

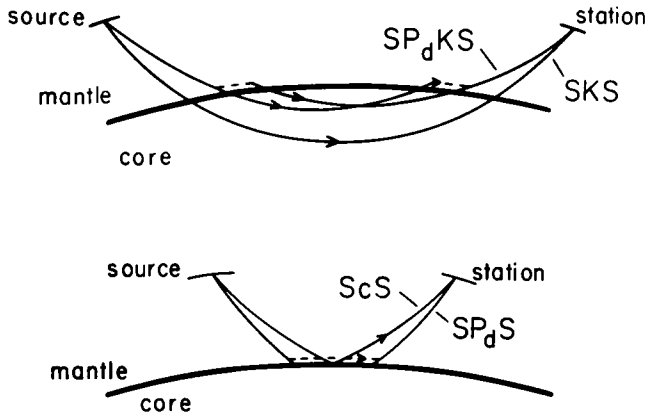

Figure 6. Top: *SP*(diff)*KS* begins as *S* and ends as *S*. In between, the path is comprised of a diffracted *P* and a *P* propagating in the core. There are an infinite number of combinations of *P*(diff) and *P* rays in the core which traverse the same arc distance. Two such paths are shown. Bottom: *SP*(diff)*S* travels first as a shear wave and then is converted to a *P*(diff) wave. The latter is eventually refracted upwards again as an *S* wave.

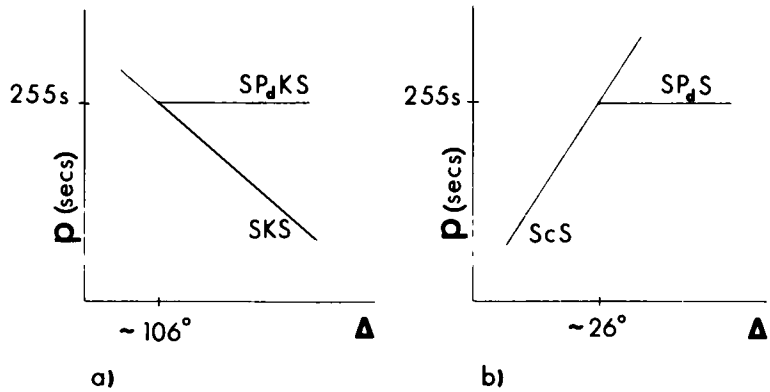

Figure 7. A diffracted ray has a constant real ray parameter as it propagates. (a) The p--Δ relationship of *SKS* and *SP*(diff)*KS*. (b) The p- Δ relationship of *ScS* and *SP*(diff)*S*. Since the travel time is the area under a p Δ curve, it is obvious that *SP*(diff)*KS* arrives behind *SKS*, while *SP*(diff)*S* is a precursor to *ScS*. For p greater than the core grazing value of 255.0 s no diffracted energy arises.

Theoretical seismograms are shown for several distances in Fig. 8. In the left column are the body-wave displacements. The ray with the critical ray parameter of 255.0 s traverses a distance of about 106°. But the distance at which *SP*(diff)*KS* is visually separable from *SKS* is about 109°. *SP*(diff)*KS* can be followed more easily as distance increases. These displacements are convolved with an instrument response of a long-period 15–100 s seismograph and the results shown on the right column. The filtering effect of the instrument obscures the arrival of diffracted energy till about 112°. When recognized as such, diffracted energy can easily be seen to arrive after *SKS* as distance increases. In practice, the most significant correction to displacement other than the instrument response is due to the finite source duration, which is characteristically 5 s for the earthquakes studied. Synthetic seismograms will be compared with observed seismograms in Figs 18 and 19, and the interpretation of the synthetic seismograms is reserved for later discussion.

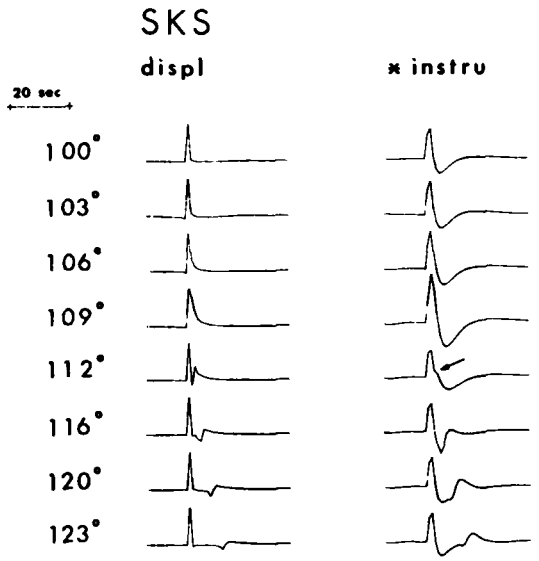

Figure 8. Theoretical waveforms of long-period *SKS* for a source depth 551 km, using earth model 1066B. In the left column is the horizontal displacement of *SKS* for various distances. *SP*(diff)*KS* can be distinguished beyond 112° but may be traced as far back as 106°. The peak amplitudes of the displacement for all distances is normalized to the same height. If normalized to the first record, the relative amplitudes would be: 1.00 at 100°; 0.30 at 103°; 0.52 at 106°; 0.27 at 109°; 0.37 at 112°; 0.38 at 116°; 0.33 at 120°; and 0.30 at 123°. In the right column are the seismograms of *SKS*, which are simply the displacements of the left column after being convolved with the instrument response of a 15 -100 s seismograph. *SP*(diff)*KS* can only be traced as far back as 112° (arrow) because of the filtering effect of the instrument.

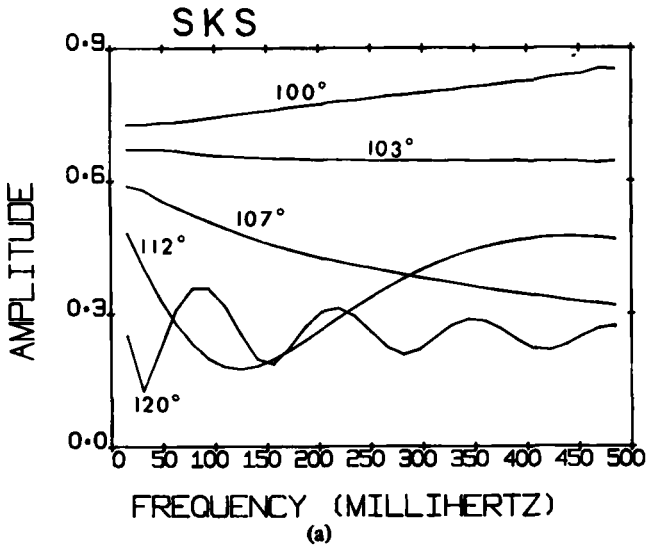

Figure 9. (a) The amplitude spectrum of *SKS* as a function of frequency for several distances. Note that for $\Delta < 103°$, amplitude increases with increasing frequency. On the other hand, for $103° < \Delta < 106°$, amplitude decreases as frequency increases. Beyond 106°, the amplitude is modulated due to the proximity of *SP*(diff)*KS* to *SKS*. (b) In order to compare the frequency dependence in the group delay for several distances, the travel-time ramp is first removed from the phase. This is equivalent to removing the ray theoretical group delay from the group delay given by full wave theory. The relative group delay that results is plotted as a function of frequency. (c) Phase delay as a function of frequency for several distances.

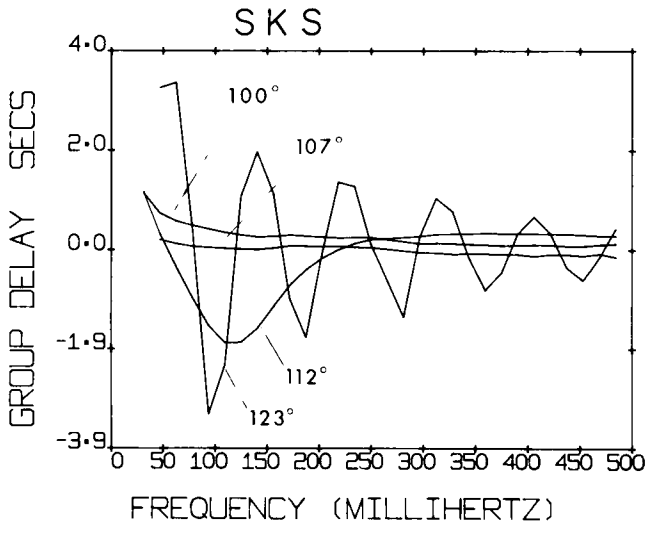

(b)

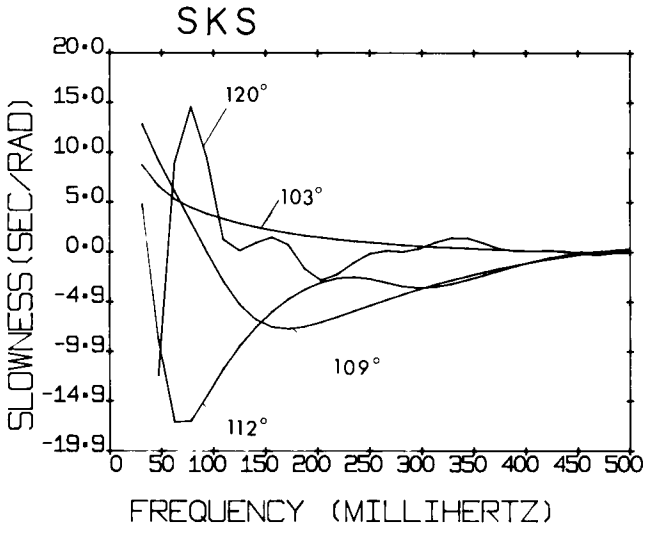

(c)

The amplitude spectra of *SKS* for several distances is shown in Fig. 9(a). Not only are the spectra obviously frequency dependent, but the character of the dependence varies. Starting at 107°, as distance increases the modulation in each spectrum increases. This is caused by the onset of *SP*(diff)*KS* energy and its proximity to *SKS*. The curve for 120° displays clearly two properties of diffracted energy. First, its proximity to *SKS* causes modulation of its spectra. Second, diffraction is strongest for the lowest frequencies. Indeed, as frequency increases, the amplitude of the modulation decreases till the flat spectrum of ray theory is approached. Another characteristic of the *SKS* spectra can be distinguished by comparing the abrupt change in the relative amplitude of low frequencies to high frequencies at distances before the onset of diffracted energy. At less than approximately 103°, the amplitude level at the low-frequency end of the spectrum is decidedly lower than the high-frequency

end. The opposite phenomenon, low-frequency amplitudes being greater than high-frequency amplitudes, is true for distances greater than 103° (but before the onset of diffracted energy). The reason for this behaviour is evident from studying the combined transmission coefficient $T_{SK}T_{KS}$ (Fig. 2). The ray parameter 255 s is the value at which a mode-converted *P* wave is refracted supercritically at the core–mantle boundary. According to ray theory, there is not only a sharp jump in amplitude and phase near this value, but it is also supposed to be frequency-independent. For finite frequencies, the amplitude and phase of transmission changes smoothly across the critical ray parameter. The frequency-dependence at less than roughly 255 s ($\Delta \geqslant 103°$) shows distinctly that the finite low frequencies have greater amplitude than the high frequencies. The reverse is true of p roughly greater than the critical ray parameter.

If frequency-dependence is ignored, defining the core–mantle discontinuity on the basis of *SKS* amplitudes could result in a gross misinterpretation. The observation of a smooth transition of amplitudes in *SKS* at finite frequencies would be interpreted by ray theory as the result of a smooth velocity gradient rather than a sharp one. Fortunately, a variety of other data (e.g. *PcP, PKP*) give complementary evidence that the core–mantle discontinuity is indeed sharp. Of course, this may not be the case in other regions of the Earth, such as the discontinuities of the upper mantle, for which there is not such a variety of complementary data.

The assumption of frequency independence in the reflection/transmission coefficients of *SKS* may also have been a major defect in the method employed by Suzuki & Sato (1970) to determine Q for the outer core. Using *SKS/ScS* ratios, they obtained a Q for the outer core on the order of several hundred, whereas most other methods yield a Q of several thousand (Sacks 1971; Qamar & Eisenberg 1974; Cormier & Richards 1976). The seismograms of *SKS* that Suzuki & Sato (1970) showed were recorded at distances near 100°. This is the range at which the magnitude of the transmission coefficients for *SKS* decrease for decreasing frequency – Fig. 8(a). Since Q is very sensitive to the amplitude of the low frequencies, compensating for this effect could well raise their estimate of Q. The *SKS/ScS* method must also take into account diffracted energy perturbing the waveform of *SKS* beyond 107°, and significant diffracted energy preceding *ScS* between 30° and 40° (as described in the next section). Fortunately Q in the core can be determined in several ways (e.g. spectral ratios of *P'P'/P* and *P7KP/P4KP*). Such a variety of complementary techniques, however, may not be available for other regions in the Earth such as the upper mantle discontinuities. The accuracy of Q in these regions might, therefore, suffer from the neglect of frequency dependence.

The techniques of ray summing, picking differential arrival times and so on assume the stability of a waveform as propagation distance increases. These methods require choosing some feature (such as a peak or trough) as a reference point, especially where the first motion of a body wave is too ambiguous to be read. Two quantities were examined, the group delay, $\partial\phi/\partial\omega$, and the phase delay, $(1/\omega)(\partial\phi/\partial\Delta)$, where ϕ is phase. In ray theory, these quantities are zero (since the ray arrival time is our choice of reference). Group delay is the slope of the phase spectrum and is a measure of the lead or lag of each frequency component in the waveform. In Fig. 9(b), the group delay of ray theory is subtracted from that of full wave theory and the resulting relative group delay is plotted as a function of frequency for several distances. At distances less than 106°, the group delay of *SKS* deviates slightly from zero only at the low-frequency end, for which the non-ray theoretical interaction at the core–mantle boundary is expected to be pronounced. The group delay curves appear modulated beyond 106°, where *SP*(diff)*KS* begins to appear with significant energy. Because diffraction is mostly a long-period phenomenon, the magnitude of the group delays approaches the ray theory value of zero as frequency increases.

Phase delay is an indication of changing waveform with distance. Apparent slowness, $dT/d\Delta$, may differ from the ray theory slowness, p, in a frequency-dependent manner (Johnson 1967):

$$\frac{dT}{d\Delta} = p + \frac{1}{\omega}\frac{\partial\phi}{\partial\Delta}. \tag{19}$$

After subtracting out the ray theory value from apparent slowness, the resulting phase delays, $(1/\omega)(\partial\phi/\partial\Delta)$, for *SKS* at different distances are plotted in Fig. 9(c). At all distances, the delays at high frequencies tend to the ray theory value of zero by 0.5 Hz. The time-domain signals (Fig. 8) show that the peak following *SKS* is due predominantly to *SP*(diff)*KS*. Since *SP*(diff)*KS*, has a different travel-time curve than *SKS*, its changing proximity to *SKS* with each distance causes drastic changes in the shape of the phase delay curves at each distance in Fig. 9(c).

In the numerical integration the contributions of *SKS* and *SP*(diff)*KS* cannot be readily separated. An idea of how the group and phase delays of *SKS* by itself behave can be seen at distances before *SP*(diff)*KS* develops ($\Delta < 106^\circ$). Frequency dependence of amplitude and phase is seen to be strongest at less than 0.20 Hz. At less than 0.20 Hz group delay deviates from ray theory by less than 1 s, so ray theoretical assumptions of choosing the arrival time of long-period *SKS* are not gravely affected by frequency dependence. Phase delays at less than 0.20 Hz deviate as much as 10 s from ray theory and might produce an error in phase velocity as high as 1 km/s. Note that the passband of WWSSN long-period seismographs favours frequencies less than 0.20 Hz.

5.2 SHORT-PERIOD *SKS*

Attenuation, scattering, and crustal response of very fine structure cannot be readily ignored in the synthesis of short-period seismograms. The displacement of *SKS* is synthesized in the left column of Fig. 10. The theoretical seismograms (right column, Fig. 10) are obtained by passing the displacements through the instrument response of a 1 -0.75 s seismograph, typical of the short-period WWSSN seismograph. *SP*(diff)*KS* is a persistent feature between 107° and 114°. Since the energy of diffraction favours the low frequencies much more than the high frequencies, it is not surprising that short-period *SP*(diff)*KS* does not persist for as great a distance as long-period *SP*(diff)*KS*. Observed short-period seismograms (Fig. 11), unfortunately, contain coda of such complication and variable duration that any identification of *SP*(diff)*KS* is very dubious without array techniques.

Any synthesis of short-period *SKS* must explain the highly variable character of the initial pulse shapes of each record in Fig. 11. For example, the time width of the first pulse of *SKS* at some stations (e.g. BLA) can be twice that at other stations (e.g. QUE). Another characteristic that varies with each record is the relative amplitude of the first peak of *SKS* to the second peak. At some stations the first peak is higher, while the reverse is true at other stations. These variations in pulse shape are distributed in no consistent pattern with distance or azimuth. Thus, they are not likely due to source effects (e.g. complex rupturing), radiation pattern or finite source duration.

Nevertheless, it is interesting to examine the effect of different source functions on the short-period displacements of *SKS*. While satisfactory for long-period *SKS*, the 5-s box-car is a woefully inadequate directivity function for short-period *SKS* – Fig. 12(a). The stopping phase is enormous and certainly not seen in the actual seismograms. The application of other time functions to the same seismogram is shown in Fig. 12(b) and (c). With the appropriate source function, a large range of relative heights between the first and second peaks of the

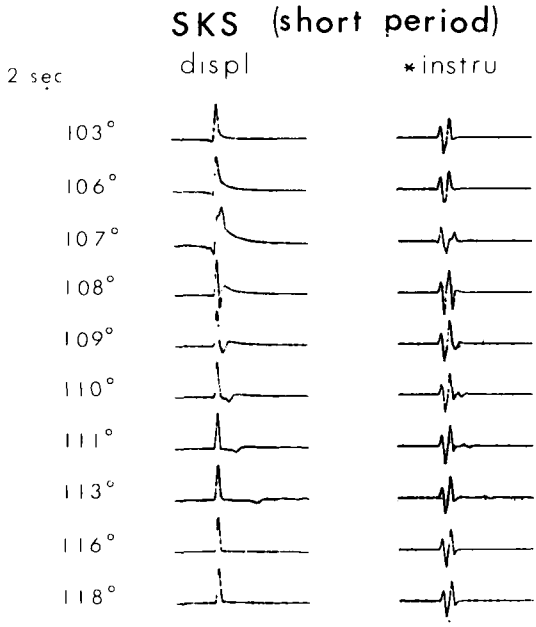

Figure 10. Short-period records of *SKS*, using model 1066B. In the Fourier inversion we use 32 frequency components with a Nyquist frequency of 4 Hz. In the left column are the horizontal displacements. In the right column are shown the displacements after they have been passed through the instrument response of a 1–0.75 s seismograph which is typical of the WWSSN short-period instruments.

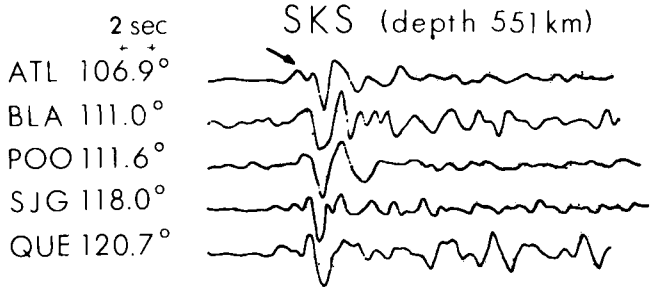

Figure 11. Short-period seismograms of *SKS* from WWSSN stations for the earthquake of 1971 November 20, depth 551 km. In each case, the east- west component is shown because it is the more radial of the horizontal components. Note that the initial pulse shape is very variable. For example, the pulse width of the initial pulse at BLA and POO is nearly twice the duration of that found in the records of SJG or ATL. The relative heights between the peaks of the initial pulse are also very variable (e.g. compare ATL with QUE).

SKS pulse can be obtained. In no case, however, does it seem likely that convolving with the time function could broaden the time width of the pulse, which is required at some stations.

Attenuation is not a likely explanation for variations in pulse width. Simulations of attenuation effects on short-period body waves (Mereu, Simpson & King 1974; Kennett 1975) claim to show that the primary effect of introducing non-dispersive finite Q in the upper mantle is to reduce the overall amplitude of a body wave. Even if material dispersion does occur, pulse broadening would only be around 1 s (Gladwin & Stacey 1974, equation (1)) and the relative height of the first two peaks would remain almost unchanged.

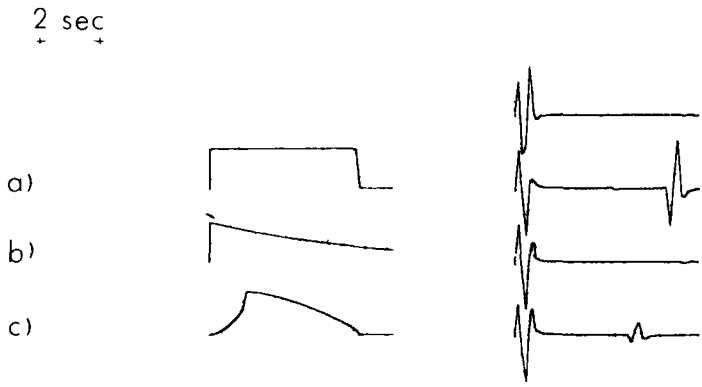

Figure 12. The effect of different source functions on a theoretical record of short-period *SKS* at 106°. The top record on the right shows the original theoretical seismogram. Beneath it are the seismograms which result after applying different source functions. In the left column are the source functions which are used: (a) a box-car, (b) an exponentially decaying function (Haskell 1964); (c) two parabolic functions (Sato & Hirazawa 1973). The relative height of the first two peaks of *SKS* can be made to vary greatly with the appropriate source function.

Crustal reverberations might explain the random distribution of pulse widths and peak amplitudes. Reverberations arriving at the time of the second peak of *SKS* might add constructively or destructively to result in records with peaks of varying heights. The proper constructive interference might also give the appearance of doubling the width of the first half cycle of the *SKS* pulse.

An arrow at the seismogram from ATL (Fig. 11) points to what may be a precursory arrival to *SKS*. It is not likely to be caused by scattered *S* energy because of its early arrival time. It must arise from mode conversion of *SKS* to a faster velocity *P* wave at some point along the propagation path. The conversion might originate from structure near the source or receiver. An *S* to *P* mode conversion at the receiver crust can be ruled out for two reasons. First, a search of the observed records showed no arrivals on the vertical component at the time of the precursor, which implies it is mostly *S* energy. Second, any reverberation at the receiver of predominantly *S* energy can be excited only by the arrival of *SKS*. Thus, the reverberation can arrive no earlier than the initial *SKS* pulse. Upper mantle discontinuities near the source are not probable causes, since the ray of *SKS* takes off steeply, and *P*-wave conversion is only slight for rays incident near normal to radial discontinuities. Since the source is deep, one remaining possibility is that a *P* wave at the source was mode-converted to *S* at the boundary of the descending slab, which is a discontinuity inclined from the vertical. In Corroboration of this hypothesis is a tendency in the data for precursory arrivals (which have no vertical component) to be seen at stations on one side of the slab, but to be absent at stations on the other side of the slab.

5.3 *ScS* AND *SP*(DIFF)*S*

ScS has no turning point, so a path of integration, Fig. 1(b), is oriented roughly normal to that used for body waves with turning points. However, as in the case of *SKS*, the contour takes account of the contribution of the diffraction poles near the real p of 255.0 s. At some distances, the contribution of the residuals included in the integration is not insignificant and the total body wave thus represented in the calculation is the combination of *ScS* and what may be called *SP*(diff)*S*. Fig. 6 (bottom) is a schematic of the rays *ScS* and

SP(diff)*S*. The $p-\Delta$ relationship of *ScS* to *SP*(diff)*S* shows that the latter is always a precursor to *ScS* – Fig. 7(b).

Theoretical seismograms of *ScS* between 20° and 50° are shown in Fig. 13. For a depth 551 km, the theoretical distance where the mode-converted *P* wave grazes the top of the core is about 27°. It is not, however, until about 30° that *SP*(diff)*S* arrives sufficiently in front of *ScS* to be distinguished from it. The amplitude of *SP*(diff)*S* decreases steadily till it is no longer visible beyond approximately 42°. The influence of instrument correction on the displacement is to spread the precursory pulse out and into the arrival of *ScS*. In the distance range 30°–40°, *SP*(diff)*S* + *ScS* arrive at the same time as a multitude of other arrivals (e.g. *sS*, *SS*, *SSS* and Rayleigh waves). Because of the complicated interference of body waves, no satisfactory observations of *SP*(diff)*S* were found. Array stacking would be one way of verifying the existence of *SP*(diff)*S* in actual data.

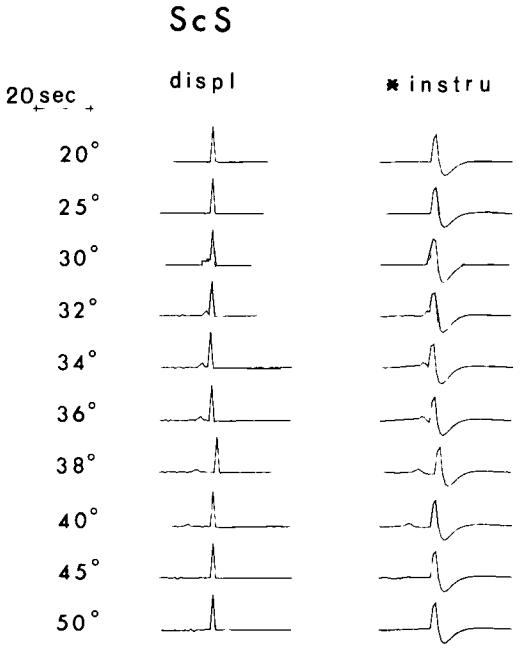

Figure 13. Theoretical seismograms of long-period *ScS* for a source depth 551 km using model 1066B. In the left column are the horizontal displacements of *ScS* for several distances. The maximum amplitude of each record is normalized to the same height. If normalized to the first record, the relative heights would be: 1.00 at 20°; 0.84 at 25°; 0.47 at 30°; 0.45 at 32°; 0.45 at 34°; 0.43 at 36°; 0.44 at 38°; 0.43 at 40°; 0.45 at 45°; and 0.49 at 50°. In the right column are the same displacements after being corrected for the instrument response of a 15–100 s seismograph.

5.4 *SKKS* AND *SmKS* ($m \geq 3$)

Between 100° and 125°, the saddle points of *SKKS* on the real p axis range from 408 to 360 s. The saddle points of the higher order multiples of *SmKS* are all squeezed between 437.5 and 417 s. Suitable paths of integration are shown in Fig. 1(c). For low frequencies ($f \leq 0.25$ Hz) the path must enclose diffraction poles associated with the ray parameter of the core-grazing *S* wave. For high frequencies ($f \geq 0.25$ Hz), contributions to the displacement integral become negligible long before the integration path comes near the diffraction poles. Thus, a shorter path of integration (Fig. 1(c), dashed line) may be chosen to reduce computation time.

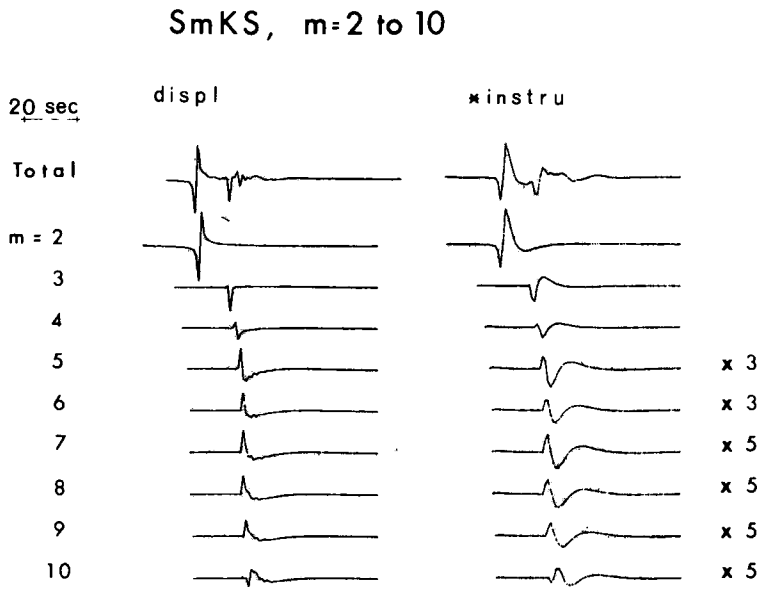

Figure 14. The relative amplitude of the waveforms of *S2KS* to *S10KS* are compared for a record at 116° with source depth 551 km. The first record in the left column is the horizontal displacement of *SmKS* summed from $m = 2$ to $m = 15$. Beneath it are its components from $m = 2$ to $m = 10$. For $m \geqslant 5$, the amplitudes of the waveforms are so small that they have to be multiplied by a factor of three or five in order to be seen. In the right column are the seismograms, which are the displacements convolved with the instrument correction of a 15–100 s seismograph.

The relative amplitudes and waveforms of *S2KS* to *S10KS* are shown in Fig. 14. The body-wave displacements (left column) and the seismograms (right column) show that *S2KS* has the largest amplitude of the group. *S3KS* and even *S4KS* are significant, but the succeeding multiples are so small that they must be magnified three to five times in the figure to make them visible. Summing the contribution of *S2KS* to *S15KS* produces an adequate displacement record. The addition of more multiples produces no perceptible effect on the body-wave displacement.

Theoretical seismograms of *SmKS* ($m \geqslant 2$) are shown in Fig. 15. The displacement (left column) shows that *SKKS* always has an emergent onset, caused by its touching an internal caustic during propagation through the Earth. *S3KS* and *S4Ks* begin to emerge from the coda as distance increases but their identity is obscured after the displacements are passed through the response of a long-period seismograph (right column). Comparison of synthetic and actual seismograms (Figs 18 and 19) is discussed in the next section of this paper.

Fig. 16 shows that, as frequency increases, *SKKS* tends asymptotically to a DC level for amplitude and to nearly zero for group delay and phase delay. The approximate point in the low-frequency end of the spectra at which amplitude and phase begin to deviate noticeably from ray theoretical values is governed by the proximity of the turning points of *SmKS* to the core–mantle boundary. To see why this is so, note that the transmission coefficients of *SmKS* are $(T_{SK}T_{KS})R_{KK}^{m-1}$, so the combined transmission coefficient of Fig. 2 is applicable to describe *SmKS* behaviour. At roughly $p = 390$ s in Fig. 2, the finite frequencies begin to deviate from the plane-wave coefficients. This corresponds to a distance of about 112° for *SKKS*. Indeed, for $\Delta \geqslant 112°$ (or $p \leqslant 390$ s), the amplitude and phase delay of *SKKS* is nearly frequency-independent. Yet at distances less than 112°, the spectra of *SKKS* display marked frequency dependent behaviour in the low-frequency end of the spectra. The curves

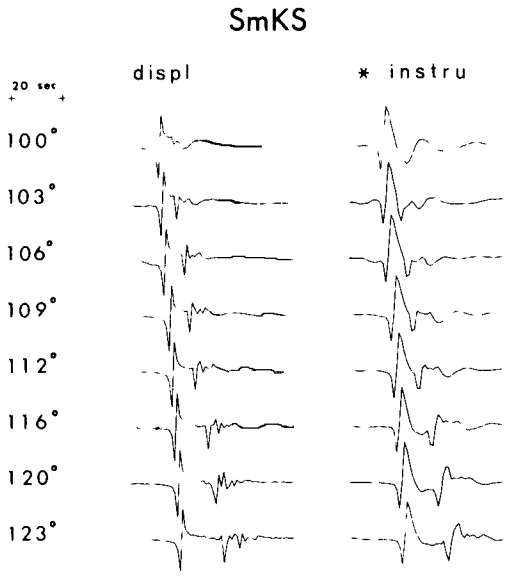

Figure 15. Theoretical waveforms of long-period *SmKS* ($m \geq 2$) for a source depth of 551 km, using model 1066B. In the left column are the horizontal displacements of *SmKS* for several distances. The maximum amplitude of each record is normalized to that of the first record. *S3KS* and even *S4KS* can be seen to separate themselves from *SKKS* as distance increases. In the right column, these displacements have been convolved with the response of a 15–100 s instrument to give the theoretical seismograms. The filtering effect of the seismograph obscures the distinctness of *S3KS* and *S4KS*.

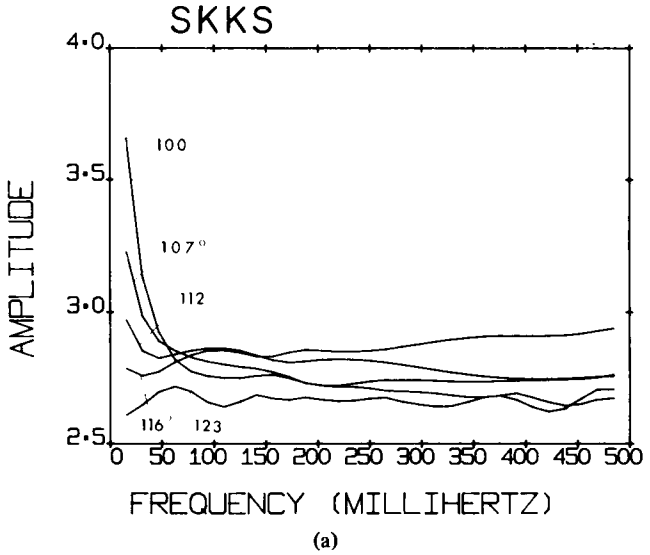

(a)

Figure 16. (a) The amplitude spectra of *SKKS* as a function of frequency for several distances. For *SKKS* with ray parameter greater than 390 s ($\Delta \leq 112°$), the low-frequency end of the spectrum is noticeably affected by the frequency dependence of the reflection/transmission coefficients. (b) The group delay as a function of frequency of *SKKS* for several distances, calculated as described in Fig. 9(b). (c) Phase delay of *SKKS* as a function of frequency for several distances.

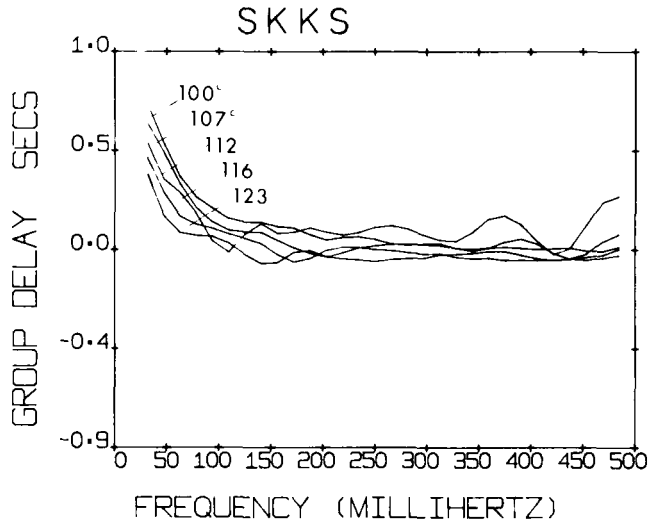

(b)

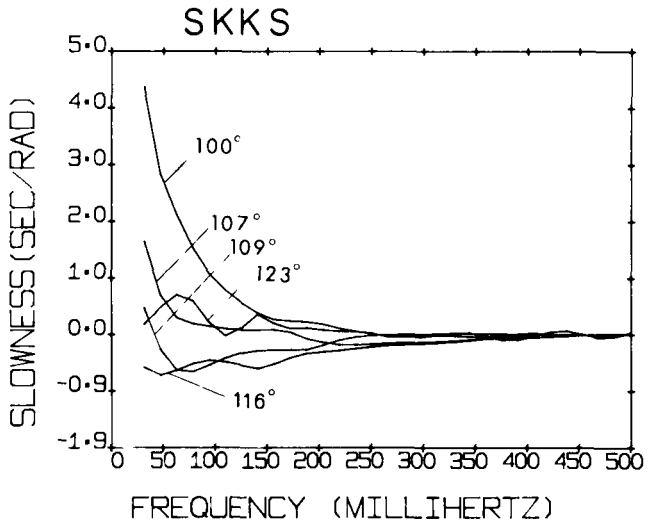

(c)

for higher multiples of *SmKS* are similar to that of *SKKS*, differing only in that the frequency dependence gradually shifts to higher frequencies. The turning points of *S3KS*, for instance, happen to be much more near the core–mantle boundary than *SKKS* for a given distance, so the amplitude spectra of *S3KS* curve upward at a higher frequency than *SKKS* (Fig. 17).

Though the integration path of *SmKS* encloses the *S* diffraction poles, no modulation in the amplitude and phase comparable to that which affected *SKS* is seen for *SKKS* or *S3KS*. Thus, we conclude that body waves of the type *S*(diff)*mKS*(diff) are not significant.

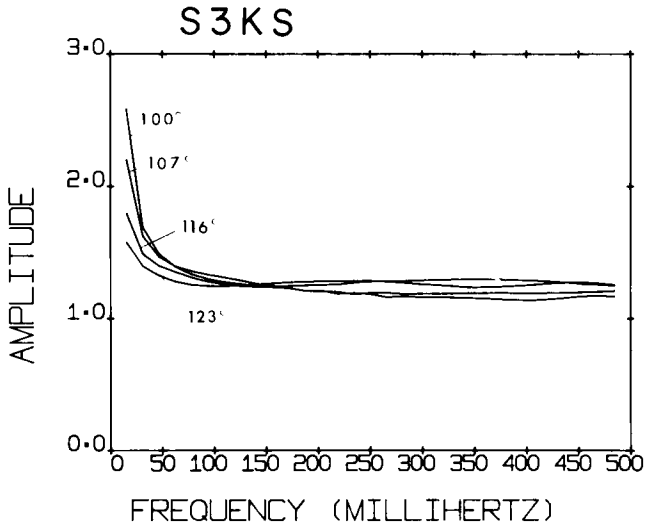

Figure 17. The amplitude spectra of *S3KS* for several distances. Between 100° and 125°, *S3Ks* has real ray parameters greater than 417 s. Thus, all amplitude spectra in this figure exhibit pronounced non-ray theoretical behaviour at the low frequencies.

6 Discussion

6.1 NATURE OF THE CORE–MANTLE BOUNDARY INFERRED FROM *SmKS* SEISMOGRAMS

It has been shown the velocity constraints on the top few hundred kilometres of the outer core are lacking because the travel-time data of higher order multiples of *SmKS* are largely inaccessible. For these body waves, the analysis of synthetic seismograms is a promising means of exploiting the total information present in the waveforms. Fig. 18 compares actual data from two deep earthquakes with long-period theoretical seismograms computed with model 1066B. The gross features of the actual seismograms are indeed replicated by the synthetics. For instance, knowing that *SP*(diff)*KS* exists, one can follow the separation of the secondary peak of *SKS* with increasing distances. Also, once it is known that *S3KS* can sizeably influence the coda of *SKKS*, its progress can be followed with distance as well. But it is through the incongruences between the observed and theoretical displacements that the deficiencies of a given model can be unearthed. There are two obvious discrepancies in the seismograms computed from 1066B. First, the time measured between peaks of *SKS* and *SKKS* is not the same for the synthetic and actual records. This causes some difficulty in aligning them. The discrepancy becomes noticeable near 114° and worsens with increasing distance. The second type of discrepancy appears in the coda of *SKKS*, which is in fact the sum of the higher multiples of *SmKS*. The interference pattern of higher multiples beyond 114° displays a prominent bump behind *SKKS* in the synthetic records which finds no comparative feature in the observed records.

The gross features of currently accepted earth models are in remarkable agreement, differing only where fine structure is concerned (Dziewonski 1976). The most significant such region encountered by *SmKS* body waves from deep earthquake sources is the core–mantle boundary. Since velocities and densities at the base of the mantle and the top of the core are yet to be satisfactorily constrained (Bolt 1972), the resolution of the discrepancies described

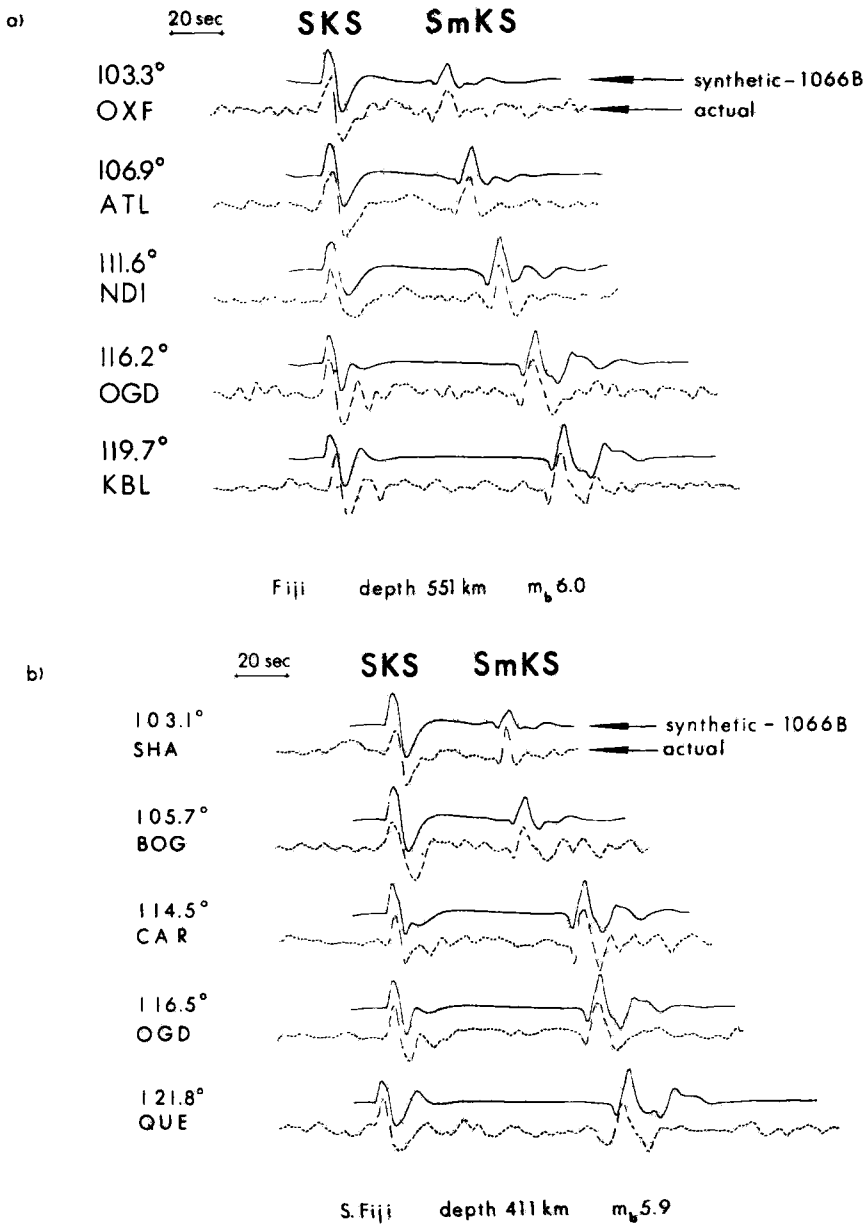

Figure 18. Observed records (dotted lines) obtained from long-period WWSSN stations are compared to synthetic records (solid lines) computed from model 1066B. the records are not aligned using the absolute arrival time predicted by an earth model with the arrival time of the observed body waves. Rather, we superimpose the actual and synthetic records till the best visual alignment between the first peaks of *SKS* and *SKKS* is obtained. This avoids the necessity of correcting for any baseline error (Jordan & Anderson 1974). We emphasize that the time interval between the peaks of *SKS* and *SKKS* should be called a reference travel time rather than a differential travel time. Remember that the waveform of *SKKS* is phase distorted upon touching an internal caustic. (a) Record sections for the earthquake of 1971 November 20, depth 551 km and m_b 6.0. All observed seismograms are the east–west components, which are nearly radially oriented with respect to the epicentre. (b) Records for the earthquake of 1973 July 21, depth 411 km, m_b 5.9. Again, the east–west components are shown because they are oriented practically in the radial direction with respect to the epicentre.

above is expected to contribute most to the understanding of this boundary. We would like to determine what properties a model of the core–mantle boundary must have in order that its theoretical seismograms correlate satisfactorily with actual records. Unfortunately, the theory of body-wave pulse propagation is not yet advanced to permit the application of generalized inverse theory. Rather than test an innumerable number of feasible models, we adopt the following strategy: a starting model (1066B) is chosen, a velocity or density is varied slightly in a narrow region of the earth (with all other parameters being held constant); and the sensitivity of the entire seismogram to each slight change is evaluated visually. For example, to test the importance of the velocity in the top 200-km of the outer core, new velocities would be inserted at the appropriate radii in the starting model. All the other values of density and velocity in the earth model would remain fixed. The sensitivity of this change is judged by comparing the waveforms predicted by the new model with those of the starting model, as well as with those of the actual data.

The number of perturbations for the parameters that we test is so numerous that in lieu of listing the velocity and density profiles of each model, we merely state qualitatively the type of changes that are to be examined. For P or S velocities, different gradients (negative, positive and zero) are tested in the 200-km at the base of the mantle or the top of the core. Each gradient is tried twice, once with velocities higher and then with velocities lower than that found in the original 1066B at the same radius, though the magnitude of the velocities never differ by more than 0.2 km/s from the original 1066B values for the same radius. Similarly, various gradients of density are tested for the 200-km on either side of the core. The density values do not differ from the 1066B values by more than 0.2 g/cm^3 in the mantle and not more than 0.5 g/cm^3 in the core. To reduce the number of combinations we must consider, the core radius for each perturbation of 1066B is kept fixed at 3485 km, which is the best radius for the core indicated by current travel-time and normal mode data (Dziewsonki & Haddon 1974).

The results of testing each type of perturbation in long-period seismograms is summarized below:

(a) Virtually no changes in waveform of the coda behind *SKKS* is produced by any of the earth models in which P or S velocities at the base of the mantle are varied. For S velocities, the reason for the insensitivity is that all *SmKS* rays, by virtue of their steep takeoff angles, traverse nearly the same path in the mantle. Consequently, each multiple reflection suffers nearly the same amplitude and phase modification irrespective of what S velocities are used. When P velocities are perturbed, the only significantly affected component of the *SmKS* body waves is *SP*(diff)*KS*, which, of course, is not a part of the coda behind *SKKS*.

(b) In contrast to the above, dramatic changes in waveform accompany minute perturbations in the P velocities of the outer core. For instance, the prominent bump in the coda behind *SKKS*, which was a disturbing prediction of 1066B for seimograms at distances greater than 114° (Fig. 18), no longer appears in the theoretical seismograms of Fig. 19. The latter seismograms are generated from a model, 1066B′, in which the P velocity of 1066B is replaced with the corresponding velocities of the JB model in just the upper 200-km of the outer core (see Table 4). The JB velocities are faster than the 1066B velocities at the same radius, but never by more than 0.1 km/s. The sensitivity of the waveforms to such minute perturbations is not surprising. We can imagine from Fig. 4 that as the order of *SmKS* increases, the rate at which the turning points approach the core–mantle boundary is initially very rapid. For instance, at 125°, the turning point of *SKKS* is about 350 km from the top of the core; that of *S3KS* is about 200 km; that of *S4KS* is about 75 km; and so on. Thus, the propagation paths of the first several multiples of *SmKS*, while almost identical in the mantle, sample quite different regions of the core.

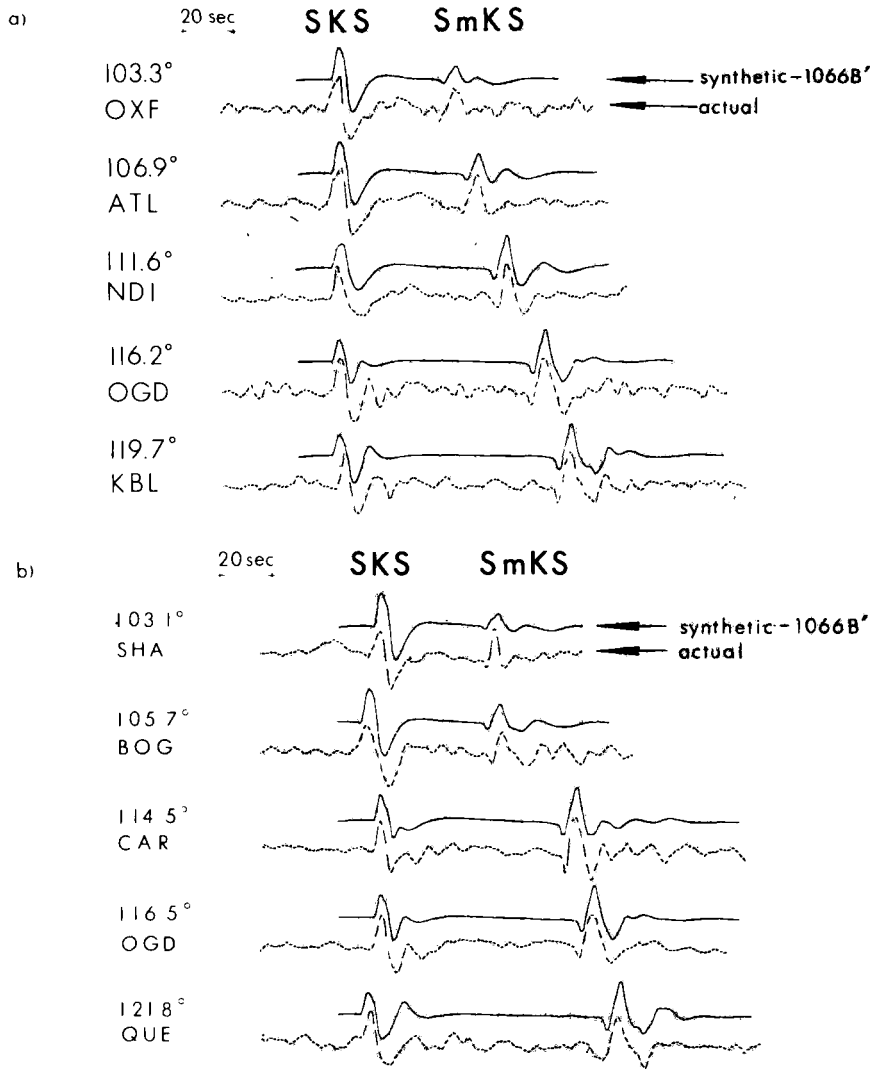

Figure 19. Observed records of Fig. 18 are now compared to the synthetic seismograms computed from model 1066B' (Table 4). (a) Records for the earthquake of 1971 November 20. (b) Records for the earthquake of 1973 July 21.

Table 4. The synthetic seismograms of Fig. 19 are generated by using a modified model of 1066B, denoted as 1066B'. It is obtained by merely replacing the velocities in the upper 200 km of the outer core of model 1066B with the velocities of the JB model. The new velocities are higher than the original ones, though the gradient is actually smaller in the JB model. Densities remain unchanged. (Note that the radius of the core in the JB model is at 3473 km, while that of the 1066B model is at 3485 km.)

Layer No.	Radius (km)	*P* velocity (km/s) 1066B	*P* velocity (km/s) 1066B'	Density (g/cm^3)
66	3485.5	7.967	8.10	9.977
65	3414.1	8.110	8.18	10.088
64	3343.1	8.243	8.26	10.189
63	3272.2	8.368	8.35	10.280
62	3201.3	8.489	8.489	10.365

(c) No visible changes in the relative time measured between the first peak of *SKS* and the first peak of *SKKS* are seen in any of the theoretical seismograms computed from models with perturbations of the *P* or *S* velocity at the base of the mantle. The reasons for the failure to produce a change are similar to the reasons why the coda of *SKKS* is insensitive to mantle velocities. By traversing nearly the same paths in the mantle *SKS* and *SKKS* sample the same *S* velocity profile and so maintain nearly the same temporal relationship with each other. Furthermore, only the *P*(diff) part of *SP*(diff)*KS* is significantly affected by a change in the mantle *P* velocities. However, the propagation distance of *P*(diff) is too brief for significant differences in propagation phase to develop when applying models with only slight velocity differences.

(d) The relative time between the first peaks of *SKS* and *SKKS* is, on the other hand, very sensitive to the *P* velocity in the outer core. As an example, we again compare the seismograms generated from 1066B′ (Fig. 19) and the seismograms generated from 1066B (Fig. 18). The relative times predicted by 1066B′ agree with the actual data better than do the synthetic records of 1066B. The reason for the sensitivity is that the propagation paths in the core of *SKS* and *SKKS* are sufficiently different that the temporal spacing between the two body waves may rapidly differentiate with even small changes in the velocities of the outer core. Note that beyond 120° the relative time between peaks in Fig. 19 still disagrees with the actual data. Beyond this distance, the turning points of *SKKS* is so deep that the ray samples portions of the core whose velocities have not yet been tested. It may be that higher velocities are required for perhaps the upper 300-km of the outer core instead of the 200-km modified thus far in 1066B′.

(e) Neither the waveform nor the arrival time of *SP*(diff)*KS* is sufficient to determine whether the *P* and *S* velocity gradients at the base of the mantle are negative or positive. The waveform of *SP*(diff)*KS* is not sensitive at all to any *P* and *S* velocity perturbations at the base of the mantle or the top of the core, for the reason that the propagation distance of *P*(diff)*K* in the vicinity of the core–mantle boundary is too brief to allow noticeable differences to develop when using models with only slight velocity differences. Furthermore, by arriving behind *SKS*, the arrival time of *SP*(diff)*KS* is always indiscernible and unusable.

(f) Perturbations up to 5 per cent of the original density on either side of the core - mantle boundary have no effect whatsoever on the waveforms or arrival times of *SmKS*.

In summary, we have identified the velocities of the outer core as the strongest constraints on the waveforms of *SmKS*. An impressive match of synthetic and actual seismograms has been presented in Fig. 19. Though not a unique model by any means, 1066B′ serves a purpose in pointing out the direction a final earth model must adopt for the outer core. Namely, the velocities of 1066B and most earth models recently proposed for the outer core are presently too low and higher values such as those given by the JB model are required for the outer 200–300 km of the core. Though the velocities of 1066B′ are higher than in 1066B, the gradient in 1066B′ that we find satisfactory is of course smaller than in 1066B. Such a lower velocity gradient may diminish the importance played by stable stratification in inhibiting the regeneration of the Earth's magnetic field by a dynamo.

Though we have been unable to determine whether a negative or positive velocity gradient for *P* or *S* velocity exists at the base of the mantle, a general comment can still be made regarding the ray theory assumptions underlying most velocity inversion schemes. The curves of Figs 9(c) and 16(c) show that the phase delay at frequencies less than 0.5 Hz is strongly frequency dependent. This means that a great portion of the frequency content of a long-period body wave is to some extent frequency dependent. If the $dT/d\Delta$'s of *SKS*, for example, had been interpreted by ray theory, an overestimate of phase velocity of as much as 1 km/s at 103° would have resulted. Some investigations of *S*(diff) required a nega-